CHARACTERISTICS OF CLOUDS AND THE NEAR CLOUD ENVIRONMENT IN A SIMULATION OF TROPICAL CONVECTION

by

Ian Bruce Glenn

A thesis submitted to the faculty of
The University of Utah
in partial fulfillment of the requirements for the degree of

Master of Science

Department of Atmospheric Sciences

The University of Utah

August 2014

The University of Utah Graduate School

STATEMENT OF THESIS APPROVAL

The thesis of **Ian Bruce Glenn**

has been approved by the following supervisory committee members:

Steven Krueger	, Chair	**Oct. 25th 2013** Date Approved
Timothy Garrett	, Member	**Oct. 25th 2013** Date Approved
Courtenay Strong	, Member	**Oct. 25th 2013** Date Approved

and by **Kevin Perry** , Chair/Dean of

the Department/College/School of **Atmospheric Sciences**

and by David B. Kieda, Dean of The Graduate School.

ABSTRACT

This work presents the general characteristics of cumulus convection and the large-scale environment in a simulation of tropical precipitating convection known as the Giga-LES. A moist static energy (MSE)-based analysis is used because MSE mixes linearly and is conserved for moist adiabatic motions. The MSE-based analysis is first used to examine the properties of convection over height and amount of dilution through mixing, and a minimum dilution greater than zero is quantified. Additionally, an interesting pattern of average buoyancy over MSE and height in the simulation is revealed, possibly linked to cloudy downdrafts and mixing at the edge of clouds.

Investigating further, an MSE-based analysis is performed on selected subregions of the simulation domain, particularly the near cloud environment (NCE) of cloudy updrafts in the simulation. It is found that the NCE around all sizes of updrafts, from shallow to deep convection, contains points with properties of a subsiding shell. The dynamical importance of the evaporative-cooling driven subsiding shell has already been demonstrated in previous work studying shallow cumulus clouds. This work presents the first evidence of subsiding shells in the NCE of deep convection, and quantifies the mass flux associated with subsiding shells for different sized clouds.

With a new understanding of the NCE of active cloudy updrafts, the updrafts themselves are studied further. The work of Lin and Arakawa is discussed which clarifies how the entraining plumes of the Arakawa and Schubert parameterization should be interpreted. The physical interpretation is that they are composed of subcloud elements with similar detrainment levels that come from different cloudy updrafts. How are the subcloud elements that make up these ideal plumes distributed

throughout the cloud field? The answer to this question has implications for the viability of different techniques of cumulus parameterization. I present a new method for characterizing the dilution of a cloud with a constant fractional entrainment rate that is sensitive to the cloud's population of least diluted subcloud elements. This allows for variability in both CTH and composition of least diluted subcloud elements to be simultaneously examined over thousands of active cloudy updrafts in the simulation.

To my family, my friends, my colleagues, and my advisor. Your care and support continually buoys me up.

"Now the sun ... by its agency the finest and sweetest water is every day carried up and is dissolved into vapour and rises to the upper region, where it is condensed again by the cold and so returns to the earth."

– Aristotle, *Meteorology*, 354b 26–30

CONTENTS

LIST OF FIGURES

ACKNOWLEDGMENTS

I would like to thank Steve Krueger, Tim Garrett, and Courtenay Strong for their instruction and discussion. This material is based upon work supported by the National Science Foundation Science and Technology Center for Multi-Scale Modeling of Atmospheric Processes (CMMAP), managed by Colorado State University under coopertative agreement No. ATM-0425247

CHAPTER 1

INTRODUCTION

Aristotle's Meteorology is one of the earliest examples of a scientific analysis of clouds (Freeland, 1999). However, the modern systematic study of clouds can trace its roots to Luke Howard and his application of the Linnaean biological classification system to clouds in 1803 (Gedzelman, 1989). Simply the title of his original work, "On the modification of clouds," is telling of the conceptual breakthrough he had made. Howard argued that there were actually only a few theoretical types of cloud, and that the thousands of forms observed in the sky were simply modifications by the environment of these fundamental ideal cloud types (Howard, 1803). Today, we use his conceptualization of these types, cirrus and cumulus, for example, as a framework to understand the fundamental physical situations that lead to condensation and the formation of clouds.

Cumulus clouds are a form of moist convection that is a response to a gravitational instability in the atmosphere. A common example of the development of such an instability begins with considering a case without clouds. The ground or ocean surface absorbs shortwave radiation from the sun and the lower levels of the atmosphere are heated. Meanwhile, a deeper layer of the atmosphere cools through emission of long-wave radiation to space, and cool dense air begins to accumulate above a warmer, less dense boundary layer near the surface. Often a stable layer, a "capping inversion," separates the two regions. In many cases, the atmosphere is stable with respect to the ascent of dry air, which cools rapidly with height as the pressure drops, losing

its buoyancy. But when a rising parcel of moist air experiences net condensation through the formation of cloud droplets, it releases the latent heat of vaporization and the cloudy parcel does not cool with height as quickly as a noncloudy parcel would, remaining buoyant. In this way, the atmosphere can be stable with respect to dry convective motions, but unstable to moist convection (Wallace and Hobbs, 2006).

In such unstable cases, moist convection in the form of cumulus clouds transports warm moist air from low levels towards upper altitudes. This rising air acts like a pump, and the movement of mass upwards in narrow cumulus updrafts induces a sinking motion and compression warming in the surrounding cool environment, which reduces the initial instability (Bjerknes, 1938). Because the amount of water vapor in the atmosphere decreases with height in general, this sinking motion in the environment can cause drying at a particular level in addition to the warming.

As buoyant parcels of cloudy air rise, they mix with environmental air as it is entrained through turbulent eddies. Entrainment is defined here as the appropriation of a parcel of environmental air by a turbulent eddy that is part of a moist convective updraft. I wish to make a distinction between the entrainment and "mixing," which I will use to mean the diffusive action that eventually homogenizes the two types of air. The amount of air entrained, as well as any change to buoyancy on account of mixing, will determine the altitude to which the air will rise before it becomes nonbuoyant. At this nonbuoyancy level, much of the cloudy air is said to "detrain" and mix with the environment. The amount of water vapor in the environment can be increased through mixing with the detrained cloudy air, and the evaporation of cloud droplets causes a cooling for the environment.

The net result of these two opposing effects of cumulus convection, whether a cooling and moistening or a warming and drying, will depend on the balance of factors in a particular case. Yanai and Johnson (1993) note that in general, the vertical extent of the cumulus cloud can make a difference. They describe how "deep" cumulonimbi that extend all the way to the top of the troposphere tend to cause a net warming

and drying in their environment. In contrast, shallow cumuli that do not extend deep into the troposphere tend to cause a net cooling and moistening of their environment. They conclude that it is important to consider a spectrum of different cumulus clouds when investigating cloud-environment interactions.

The amount of air entrained by cumulus clouds is part of what determines the vertical distribution of the amount of mass and moisture that they transport in response to an instability. This transport by cumulus clouds can significantly alter the temperature and amount of moisture in the surrounding atmosphere over horizontal scales much much larger than the area of the updrafts (Bjerknes, 1938). In the context of the problem of numerical weather and climate prediction, motions on the scale of cumulus clouds are often unresolved by the large grid size of global models (Arakawa, 2004). Therefore, the net effect of the vertical transport of mass and moisture by cumulus clouds must be correctly represented for the large-scale model through a cumulus parameterization like that of Arakawa and Schubert (1974), hereafter AS74.

1.1 Entrainment and moist static energy

In a paper describing a general framework for understanding growth and decay in complex systems, Garrett (2012) begins by defining a surface of constant potential energy per unit matter. The system represented by this surface has a reservoir of energy available to it at a slightly higher potential, with the difference of potential between these two surfaces being small compared to the system potential itself. The system also has a sink at a lower potential. Any increase or decrease of mass in the system is fundamentally related to flows of material across the potential surface. Any internal complexity, such as movement of mass within the constant level of potential energy, is unnecessary to resolve because it is part of the total system which is being modeled. Only a flow of matter across the potential gradient can cause a growth or decay of the system.

A popular potential used in the atmospheric sciences is the moist static energy

(MSE). It is defined as an energy per unit mass of air that comes from adding together the gravitational potential energy via the altitude of the air, kinetic energy represented by air temperature, and the potential associated with breaking molecular bonds through the latent heat of vaporization. A parcel of air can experience variability of altitude, temperature, and water vapor content while conserving MSE. Such a process is termed "moist adiabatic." Therefore, this sum of potentials is useful because moist adiabatic variability among the three potentials is internal to the system, contained in the "step" of the constant potential surface. A full definition and discussion will follow in Chapter 2, where constant potential surfaces like those described in Garrett (2012) are defined as surfaces of constant MSE.

Because MSE is conserved for moist adiabatic processes, it can serve as a tracer for mixing in the presence of cumulus convection. Kuang and Bretherton (2006) and Khairoutdinov and Randall (2006) use the distribution of air properties over a spectrum of constant MSE surfaces and height to characterize convection in different simulations of tropical convection. Typically, the MSE in the lower half of the tropical atmosphere decreases rapidly with height. However, the MSE of a parcel of moist air will remain constant if the parcel rises without experiencing mixing. If the parcel with a high value of MSE entrains and mixes with lower MSE air from the surrounding environment, the result will be an intermediate value of MSE for the mixed parcel. In this way, it is possible to analyze the entrainment and mixing in simulated cumulus clouds by looking at how the distribution of MSE in the cloud changes with height relative to the environment.

Kuang and Bretherton (2006) note that the high values of MSE found in the low levels of their simulation are not found in the upper levels, even when deep cumulonimbus clouds are present. They conclude that the vertical flux of air undiluted by mixing is insignificant, in contrast to the "undilute hot tower" hypothesis of Riehl and Malkus (1958). Observations reported in Zipser (2003) also support the idea that even cloudy updrafts that extend from near the surface to the upper troposphere

do not contain appreciable amounts of low-level air undiluted by mixing. Fierro et al. (2009) claims to be the first study to use coordinated comparisons between observations as well as a numerical model for a tropical deep convective case to evaluate the hot tower hypothesis. Their paper, with the same second author as Riehl and Malkus (1958), concludes that undiluted ascent of air does not occur in the deep convection they studied, and redefines a "hot tower" as any convective cloud with a base in the boundary layer and a top in the upper troposphere.

To study entrainment and mixing among different types of clouds, I used the high-resolution simulation of tropical oceanic deep convection described in (Khairoutdinov et al., 2010). The simulation was performed with the System for Atmospheric Modeling (SAM) (Khairoutdinov and Randall, 2003). Constant large-scale forcing idealized from the Global Atmospheric Research Program's Atlantic Tropical Experiment (GATE) is applied for 24 simulated hours (no diurnal cycle). SAM is run as a large eddy simulation (LES), in which the grid scale is chosen to be small enough to resolve most of the turbulent eddies responsible for entrainment. The horizontal grid spacing is 100 m with a full domain size of 204.8 km by 204.8 km. There are 256 vertical levels with a spacing of 50 m in the lowest 1 km expanding linearly to a spacing of 100 m by 5 km height. Because this simulation contains one billion grid points, it is called the Giga-LES. Convection in the simulation reaches a statistically steady state after 12 hours, and all analysis is performed on the second 12 hours of the simulation. The Giga-LES domain is large enough to contain many deep cumulonimbus size clouds as well as many smaller cumulus congestus and cumulus humilis size clouds throughout their life-cycles.

Does air in tropical deep convection ascend undiluted by mixing with its environment? I will use a MSE-based analysis and the Giga-LES to answer this question. I expect based on the previously cited work to find that air does not ascend undiluted from the subcloud layer. However, some parameterizations of cumulus convection for climate models allow undilute ascent, such as that of Zhang and McFarlane (1995),

which is still used in the most recent version of the Community Atmospheric Model (CAM5) (Song et al., 2012). A cumulus parameterization that models cumulus convection as a single entraining convective plume, or as a spectrum of them, can allow undilute ascent by letting the minimum entrainment rate of the plume be zero. If undilute ascent does not occur, what minimum entrainment rate best represents the dilution that is found in tropical deep convection?

In addition to the entrainment characteristics of the cumulus convection, I will also investigate the detrainment of mass from active cumulus updrafts. The assumption in the AS74 cumulus parameterization is that cloudy updraft air detrains at the cloud top defined by the nonbuoyancy level of a convective plume with a constant fractional entrainment rate. I will refer to this type of detrainment specifically as dynamic detrainment. After de Rooy et al. (2013), I note a distinction between this dynamic detrainment and turbulent detrainment. Turbulent detrainment can occur at any level of the cloud when a parcel is ejected from the lateral boundary of the cloud, perhaps after an entrainment and mixing event with the environment. It is a quantity that will depend on the chosen definition of the boundary of the cloud. Given the turbulent nature of cumulus convection, entrainment of environmental air into a cloud can create multiple mixtures of different fractions of cloud and environment air, some of which will remain buoyant with respect to the environment, and others not. The turbulent detrainment of any nonbuoyant parcels is represented in so-called "buoyancy sorting" cumulus parameterizations such as (Bretherton et al., 2004). Turbulent detrainment of negatively buoyant parcels has been shown to form a coherent subsiding shell-like structure around shallow cumulus clouds (Heus and Jonker, 2008). Does a subsiding shell of turbulent detrainment also exist in the vicinity of deep cumulus clouds?

1.2 The subsiding shell

Recent research concerning shallow cumulus convection has revealed the existence of a structure distinct from the cloudy updraft and the cloud's environment called

a subsiding shell. Measurements from penetration of shallow cumulus convection by aircraft (Jonas, 1990; Rodts et al., 2003) show the subsiding shell as a narrow region of negative vertical velocity surrounding a convective updraft. Rodts et al. (2003) sample shallow cumulus clouds with diameters ranging from 500 m to 2500 m and composite their observations to show that the average descending shell is approximately 30% as thick as the updraft it surrounds. The dynamical importance of the structure was demonstrated by Heus and Jonker (2008), hereafter HJ08, and Jonker et al. (2008). They used the aircraft measurements of Rodts et al. (2003) to validate a large eddy simulation (LES) of shallow convection, and then analyzed the more detailed information available from the simulation to understand the mechanism behind the subsiding shell. Their highest resolution LES had a domain of $6.4\text{km} \times 6.4\text{km} \times 3.2\text{km}$ with a grid spacing of $\Delta x = \Delta y = 25\text{m}$, $\Delta z = 20\text{m}$. They identified subsiding shells as a minimum in vertical velocity existing in a near-cloud environment (NCE) region extending up to about 100m just outside the boundary of their simulated convective updrafts. They presented the budget for terms of the vertical velocity equation in the NCE, showing that the pressure gradient acceleration, advection, and the subgrid scale transport all act to increase the vertical velocity in the NCE region, which does not support the view that the subsiding shell is mechanically forced or a compensating subsidence. HJ08 showed that only the acceleration from the negative buoyancy term could explain the negative vertical velocities of the subsiding shell. Furthermore, they found that while the magnitude of the negative vertical velocity in the NCE is usually less than the average vertical velocity in the cloudy updraft, the relatively large NCE area means that the downward mass flux in the NCE is a considerable fraction of the upward mass flux in the cloudy updraft. They showed that these properties make the subsiding shell in the NCE region dynamically important and distinct from both the adjacent cloud and the large-scale environment.

Understanding the subsiding shell and the near-cloud environment is part of the key to understanding the interactions between clouds and the large-scale environ-

ment. The existence of a subsiding shell has implications for the scientific goal of cumulus parameterization, which is to describe the collective effects of cumulus on their surrounding environment without needing to predict individual clouds (Lin and Arakawa, 1997a). Entrainment and detrainment by cumulus clouds is a fundamental aspect of what a cumulus parameterization needs to provide to a climate model (Arakawa, 2004). Recent work using particle tracking in LES has shown that lateral mixing is the dominant entrainment mechanism between a convective updraft and its environment, as opposed to cloud-top entrainment (de Rooy et al., 2013; Heus et al., 2008). This lateral mixing has been the basis for a framework to explain entrainment and detrainment called "buoyancy sorting" (Taylor and Baker, 1991). Using different methods, both Romps (2010) and Dawe and Austin (2011) show that entrainment rates calculated by directly measuring parcels entering a cloud are a factor of two larger than when entrainment is estimated using a "bulk" approach and assuming the cloud mixes with air having the average environment properties. This illustrates that the properties of the NCE are different from the properties of the average environment (Dawe and Austin, 2011). In this study, we examined the properties of the NCEs of deep convective updrafts to look for evidence of a subsiding shell.

To study the properties of the NCE of deep convection, we used a high-resolution simulation of tropical oceanic convection known as the Giga-LES. The Giga-LES is one of the first simulations of tropical deep convection that is well-suited to the task of studying a small feature such as subsiding shells. The simulation grid scale is small enough to resolve most of the turbulent eddies responsible for entrainment, while the domain is large enough to contain many deep clouds.

Is the NCE like the average environment, or is it more similar to the cloud it surrounds? Are mixtures between "cloud" and "environment" air resolved in the Giga-LES, and do they have the properties of a subsiding shell? To answer these questions we defined a NCE as the region within 500 m of a 3-D cloudy updraft in the Giga-LES. We used the conserved variable moist static energy (MSE) to analyze the mixing

process in the NCEs. We find that the air in the NCE mostly contains air parcels with either cloudy updraft or environment values of MSE with a continuous distribution of values in-between that represent mixtures of the two. We then examined the distributions of relevant physical variables versus MSE and height and show that the NCEs in the Giga-LES have the properties of subsiding shells.

1.3 Clouds and entraining plumes

I identified 3-D cloudy updrafts in the Giga-LES as contiguous points with vertical velocity and cloud condensate mixing ratio greater than characteristic threshold values. The NCE analysis clarifies the utility of this definition of an individual "cloud" as a contiguous cloudy updraft region. As I show in Chapter 3, such a definition excludes both the cloudy and clear air that composes the negatively buoyant subsiding shell, while still including any part of the cloudy updraft that over-shoots its nonbuoyancy level. In this way, the chosen cloudy updraft definition approximately isolates the part of the cloud that is actively transporting mass and moisture to the upper levels. It is this transport that is traditionally represented by a cumulus parameterization in climate models (Arakawa, 2004).

The cumulus parameterization of AS74 accounts for different cumulus clouds and their effect on each other and their large-scale environment using multiple idealized convective plumes. For example, one of the effects of cumulus clouds is to induce subsidence in their-large scale environment, as discussed earlier. The AS74 parameterization defines multiple convective plumes with different fractional entrainment rates such that each has a different nonbuoyancy level, one for each model level. The plume is assumed to not detrain any mass until it reaches its nonbuoyancy level, where it is assumed to completely detrain. This detrainment of cloud mass at each level is used to find the induced environmental subsidence as a function of height using the principle of conservation of mass. In practice, this part of the parameterization as described is actually executed in reverse; a closure assumption is used to obtain a target induced

subsidence, and the plume mass flux is solved for iteratively. Regardless, the solution relies on the assumption that such a plume based model approximates the actual distribution of cloud mass flux at different dilutions and detrainment as a function of height.

Lin and Arakawa (1997b) use a CRM to track the movement of parcels of cloudy updraft air to compare the characteristics of mass flux and dilution in individual cloudy updrafts to that which is assumed to occur in the plume model of AS74. They show that the mean MSE in an individual contiguous cloudy updraft is not equal to that of an entraining plume with a similar top height. They also show that there is considerable internal variability of MSE at each height for a single contiguous cloudy updraft, in contrast to the assumption of a single value of MSE at each height for a convective plume. They claim that the variability of MSE in the interior of each cloudy updraft is due to the updraft being composed of multiple subcloud elements. They track these subcloud elements to determine the ultimate top height for each subcloud element. They group all these CRM subcloud elements that reach the same top height as a single "cloud type" and compare these cloud types to the convective entraining plumes of AS74.

The distribution of subcloud elements is such that, even though each cloud type is composed of subcloud elements that may have come from multiple distinct cloudy updrafts, the change in MSE with height can be approximated by a single convective plume with a constant fractional entrainment rate and the same ultimate top height. There are a few differences however, particularly at low levels. In general, they note the approximation is good only because of two mutually canceling factors: an assumed initial plume MSE value much lower than those observed for each grouped cloud type, and an assumed constant plume entrainment rate leading to less of a MSE reduction. It appears the cloud type groups actually have high MSE and a large entrainment rate at first in low to mid-levels, which then transitions to a weaker entrainment rate aloft, so the balancing effect of the two mutually canceling entraining plume assumptions

leads to a good approximation.

Lin and Arakawa (1997b) claim that the variability of the interior structure of different individual cloudy updrafts is due to each being a different sample of a statistical space, a "cloud spectrum" that can be well modeled given many clouds by a spectrum of entraining plumes. Their idea is that an individual plume with a constant fractional entrainment rate is composed of all the subcloud elements that have the same ultimate detrainment level as the plume. So although the mass flux of a cloud type in the parameterization is modeled by a single plume, it is interpreted to come from the net effect of different subcloud elements that are distributed throughout the cloud field.

How are the subcloud elements that make up these ideal plumes distributed throughout the cloud field? What is the distribution of subcloud elements per cloud that adds up over all clouds to form a mass flux distribution over MSE and height that is well approximated by a spectrum of plumes? Is it self-similar between all clouds, dependent on a cloud base property, or the cloud's ultimate cloud top height (UCTH)? If the answer to any of those questions is yes, the implication of cloud scale predictability would be encouraging for the ability of a cumulus parameterization to be successful over smaller horizontal domains, which is part of the so called "grey-zone" problem (Gerard, 2007). Or does the distribution of subcloud elements per cloud appear to be random, encouraging for a stochastic parameterization, but lending no support for cloud scale predictability? Could a spectrum of plumes with constant fractional entrainment rates approximate the mass flux distribution over MSE and height of an individual contiguous cloudy updraft ("cloud")? What about over the lifetime of a cloud?

I take a step towards answering these questions by examining the distribution of the least diluted parcels for individual clouds and over the lifetime of selected clouds. In Chapter 4, I examine statistics of the 3-D cloud population in the Giga-LES simulation. I attempt to interpret the statistics in the framework of the spectrum of

entraining plumes described in AS74 in order to understand how different clouds have different distributions of subcloud mass flux and MSE. As has been shown in other work (Emanuel, 1994; Lin and Arakawa, 1997b), I show that the mean cloud MSE is not equal to that of a plume with a constant fractional entrainment rate chosen such that is has a top height similar to the cloud, analogous to the Warner paradox (Warner, 1970). However, I describe a similar type of fractional entrainment rate derived in a novel way from mean cloud vertical velocity and buoyancy profiles and show that it can illustrate the variability of both cloud top height and the population of minimally diluted subcloud elements for many clouds.

Since some of the variability in the dilution characteristics of different clouds having a similar CTH could be due to those clouds having a different UCTH, I will attempt to track 3-D clouds through time. I refer to these tracked 3-D clouds as 4-D clouds, and the method used allows the UCTH to be determined for a 4-D cloud. This 4-D analysis is similar to the tracking analysis for ultimate top height of subcloud parcels done by Lin and Arakawa (1997a), although with a larger sample of simulated clouds available. Instead of analyzing all clouds right away, I present a brief analysis of a few 4-D clouds as a case study to see if the computationally intensive method warrants further investigation given its potential to answer the questions described above.

In summary, the goal of the work presented in these chapters is twofold. The first goal is to understand how the cloudy updraft mass flux in the Giga-LES is distributed through the general framework of fundamental ideas about cumulus parameterization that have been established in the field. This is done through a MSE spectrum and entraining plume-based analysis in Chapters 2, 3, and 4. The second goal for this work is to present new insight through a fresh interpretation of established analysis methods. In Chapter 3, I apply the MSE spectrum analysis in a new way that presents evidence for the existence of a subsiding shell of mass flux around deep convective updrafts. And in Chapter 4, I present a novel technique for characterizing individual

clouds with a bulk fractional entrainment rate that could lead to new answers for important scientific questions about the distribution of cloudy updraft mass flux over space, time, and dilution. Finally, in Chapter 5, I present some discussion and conclusions.

CHAPTER 2

MOIST STATIC ENERGY ANALYSIS

The moist static energy (MSE) is conserved for moist adiabatic processes. This makes it useful for analyzing mixing between cumulus clouds and their environment. The moist adiabatic processes that can change the properties of cumulus clouds, such as condensation increasing liquid water content and temperature, will not change the MSE. However, the result of mixing two parcels of air with different values of MSE will be a parcel with an intermediate value of MSE. As discussed in Section 1.1, I will use an MSE-based analysis like that of Kuang and Bretherton (2006) to evaluate the "hot tower hypothesis" of Riehl and Malkus (1958). Does air in tropical deep convection ascend undiluted by mixing with its environment? If not, what is the minimum rate of dilution?

2.1 MSE definition and frequency distribution

I will use the symbol h to mathematically represent the moist static energy (MSE) in temperature units as

$$h = T + (g/c_p)z + (L/c_p)q_v, \tag{2.1}$$

where c_p is the specific heat at constant pressure, T is temperature, g is gravity, z is height, L is the latent heat of vaporization, and q_v is the water vapor mixing ratio. Is it conserved for any dry or moist adiabatic motion? Consider the MSE of an unsaturated parcel rising without mixing. The temperature of the parcel decreases with height at the dry adiabatic lapse rate of $dT/dz = -g/c_p$ (Holton, 1992). Therefore, given a dry

adiabatic motion, the decrease in the first term on the right-hand side (RHS) of (2.1) will be exactly balanced by an increase in the second term on the RHS.

We can also consider a saturated parcel rising without mixing. As the parcel cools, the saturation value of the water vapor mixing ratio will decrease, and water vapor in the parcel in excess of the now lower saturation value will be condensed. I will not derive the moist adiabatic lapse rate, as this is covered in multiple introductory texts (Holton, 1992; Wallace and Hobbs, 2006). However, its form is such that the release of latent heat from condensation will increase the first term on the RHS of (2.1) just as much as the decrease in the third term, and the MSE will remain constant for a rising saturated parcel. Due to the "all-or-nothing" condensation scheme of the SAM model (Khairoutdinov and Randall, 2003), this process occurs instantaneously in the Giga-LES and the simulated MSE is not subject to variation due to super-saturation of water vapor.

The MSE is not conserved for freezing processes; there is no term that involves the latent heat of fusion or a measure of the ice condensate. As a check, the analysis that follows was performed a second time using a variation of the MSE that attempts to account for freezing and melting processes, the frozen moist static energy (FMSE) after Bretherton et al. (2005), which resulted in very slight changes and did not affect the conclusions. This is because the FMSE method assumes any ice condensate at a location formed at that location, which is not consistently true in the Giga-LES because it allows precipitating ice, which has a fall speed and sediments (Khairoutdinov and Randall, 2003). From the secondary analysis, it appears that the error in the approximation that the FMSE is conserved is similar to the error in the approximation that the MSE itself is conserved, so for the sake of simplicity, I only use the MSE.

In the Giga-LES, I counted the number of grid points that have similar MSE values at each height at hour 12 in the simulation (Figure 2.1). I used a bin range of $\Delta h = 0.1$ K. In Figure 2.1, the solid black line represents $\overline{h}$, the MSE averaged horizontally over the entire domain. The dashed black line is the MSE that air with

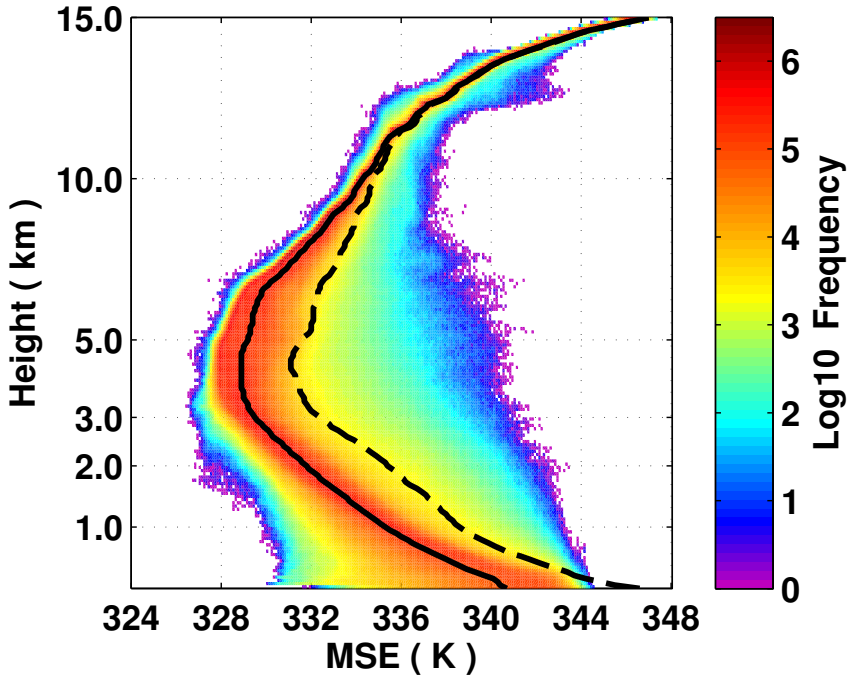

Figure 2.1. The base 10 logarithm of the frequency distribution of moist static energy (MSE) vs. height for the full domain of the LES. The MSE bin width is 0.1 K. The solid line is $\overline{h}$, the mean MSE at each height, and the dashed line is that MSE at saturation, $\overline{h^*}$.

the domain average temperature would have if it were saturated with respect to a flat surface of pure water. I refer to it as $\overline{h^*}$, defined as the horizontal average of $h^* = T + (g/c_p)z + (L/c_p)q_v^*$, where q_v^* is the saturation water vapor mixing ratio.

Figure 2.1 shows that the vast majority of points in the simulation have MSE near the mean value of MSE for each level. The points with MSE higher than the saturation value are orders of magnitude less frequent. The maximum MSE observed at any level decreases continuously with height from 344 K near the surface to 338 K at 10 km. As discussed above, the MSE of a parcel can be appreciably changed by mixing. A parcel rising from low levels without mixing would have constant MSE with height. Particularly over the range from 1 km to 10 km where the maximum MSE is far from the mean MSE, the points with the highest values of MSE represent the least diluted rising parcels. However, the decrease of maximum MSE with height

illustrates the lack of any parcels having risen undiluted from the low levels. This is consistent with observations and previous work (Zipser, 2003; Romps and Kuang, 2010a).

2.2 Entrainment rate and mass flux

It is clear that the minimum rate of dilution of deep cumulus convection is greater than zero. What is the minimum rate of dilution caused by entrainment in this tropical deep convective case? Entrainment has been defined as the incorporation of environmental air into a cumulus cloud via turbulent motion. Entrainment of environmental air by a rising cumulus cloud increases the mass of air moving upward in the cloud. The mass flux at a particular level of a cumulus cloud is $M = \rho \overline{w_c} \sigma_c$ (kg s^{-1}), where ρ is the density, σ_c is the area covered by the cloud, and $\overline{w_c}$ is the average vertical velocity in the cloud. I define the net increase of mass flux with height for a cumulus cloud as coming from a balance between a fractional entrainment and detrainment rate at the lateral boundary of the cloud,

$$\frac{\partial \ln M}{\partial z} = \lambda - \delta, \tag{2.2}$$

where λ is the fractional rate of entrainment and δ is the fractional rate of detrainment. If entrainment exceeds detrainment, the cumulus cloud mass flux will increase with height, and vice versa. How can the MSE be used to evaluate the entrainment rate? After de Rooy et al. (2013) and Siebesma (1998), I write the conservation equation for moist static energy using h_c as the in-cloud value of MSE,

$$\frac{\partial \sigma_c h_c}{\partial t} + \frac{1}{A} \oint \hat{\mathbf{n}} \cdot (\mathbf{u} - \mathbf{u_i}) h_i \, dl + \frac{\partial a_c \overline{wh}^c}{\partial z} = S. \tag{2.3}$$

In this equation A is the full horizontal area of interest including cloud and environment, $\hat{\mathbf{n}}$ is a unit vector normal to the cloud-environment interface, and $\mathbf{u}$ and $\mathbf{u_i}$ are 3-D velocity vectors of the air at the interface and of the interface itself, respectively. Therefore, with h_i as the MSE at the interface, the second term on the left-hand side

(LHS) of (2.3) represents net entrainment or detrainment of MSE. The detrained air has MSE of the cloud h_c and entrained air has MSE of the environment h_e. The over-bar with a small "c" next to it in the third term on the LHS denotes an average over the cloud, meaning the whole term represents the vertical divergence of MSE flux in the cloud. The MSE is assumed to be totally conserved so that any net source or sink $S \approx 0$. We also assume that the cloud is in steady state and any time derivative of in-cloud MSE will go to zero. Using (2.2) and the assumptions above, we can write

$$\frac{\partial a_c \overline{wh}^c}{\partial z} \approx M(\lambda h_e - \delta h_c) \tag{2.4}$$

Using Reynolds decomposition of the MSE flux term, we also have

$$\overline{wh}^c = w_c h_c + \overline{w'h'}^c, \tag{2.5}$$

where primes denote perturbations from the mean. To simplify (2.4), I will assume the last term on the right-hand side of (2.5) is negligibly small, ignoring in-cloud transport of MSE due to subcloud variability. Siebesma and Cuijpers (1995) support this "top-hat" assumption for shallow cumulus, and the same assumption is made in Arakawa and Wu (2013), although they show there are some combinations of cases of A and σ_c for which it is significant. Arakawa and Wu (2013) note that they plan to publish a method to take account of the in-cloud "eddy" transport in the future. Using the definition of the mass flux M and the above assumptions, we can simplify (2.4) to obtain an equation for the bulk fractional entrainment rate λ,

$$\frac{\partial \overline{h_c}}{\partial z} = -\lambda(\overline{h_c} - \overline{h_e}). \tag{2.6}$$

Since the assumption has been made that the bulk of the in-cloud MSE values can be represented by the single value $\overline{h_c}$, and similarly for the entrained environmental air, the λ defined in (2.6) is referred to as a bulk fractional entrainment rate. Equation (2.6) can also be derived from equation (97) in AS74.

To approximate the minimum entrainment rate in the simulation, I evaluate equation (2.6) letting $\overline{h_e}$ be the domain average MSE at each level. I choose a cloud

base value of MSE to be the initial $\overline{h_c}$, and then consider many different constant values of λ and evaluate equation (2.6) to find different profiles for $\overline{h_c}$. The λ that results in a profile of $\overline{h_c}$ that best matches the MSE of the least diluted points in the Giga-LES will represent the minimum constant fractional entrainment rate that should be used to parameterize the convection. Lin and Arakawa (1997b) note that for parcels that ascend in cumulus clouds out of the subcloud layer, their MSE is not equal to the subcloud layer average MSE, but often the maximum MSE observed in the subcloud layer. Romps and Kuang (2011) show that parcels of air that rise in cumulus clouds often originate within 200 m of the surface, or the first few model levels of a simulation.

Given this previous work and Figure 2.1, I choose an initial value for $\overline{h_c}$ at the first model level to be 344 K, and evaluate equation (2.6) for different values of λ to find different vertical profiles of $\overline{h_c}$, which are plotted in Figure 2.2. These profiles represent convective plumes with constant fractional entrainment rates of 50% km^{-1}, 20% km^{-1}, and 10% km^{-1} from left to right. The minimum fractional entrainment rate appears to be close to 10% km^{-1}. This is certainly a small value, but it is significantly greater than zero.

To understand the flux of mass occurring in the simulation at the same values of MSE as convective plumes with constant fractional entrainment rates, I also plot the mass flux over MSE and height in Figure 2.2. The mass flux in a particular bin is found by summing the vertical velocity of all points with MSE that fall into that bin range. Multiplying by the area of each grid cell gives a volume flux (m^3 s^{-1}). Multiplying this by the air density (g m^{-3}) at that level gives the mass flux in units of (g s^{-1}). To facilitate comparison with other simulations, I normalize the mass flux value by dividing by the domain area of $4.2 \cdot 10^{10}$ m ^{2} and the 0.1 K MSE bin width to give the final units of (g s^{-1} m^{-2} K^{-1}). Figure 2.2 shows that positive mass flux dominates at values of MSE near the environmental saturation value and higher, while negative net mass flux is primarily concentrated near the mean value of MSE. Following the

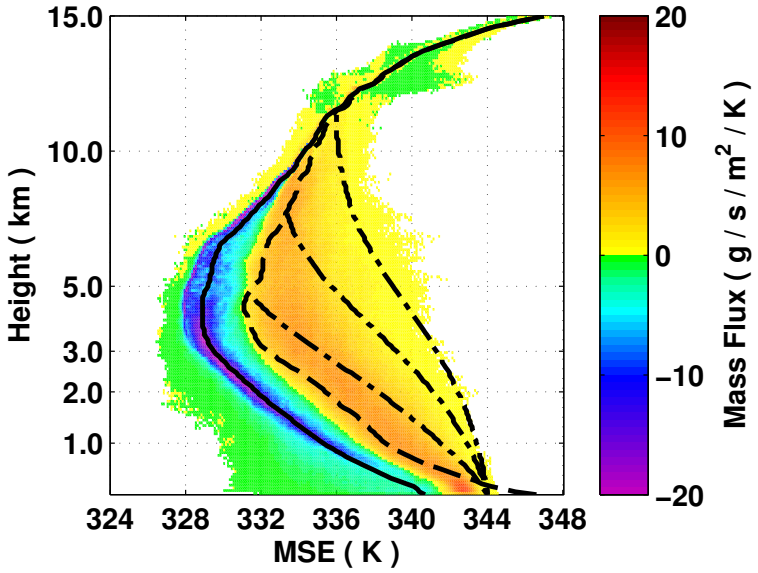

Figure 2.2. As in Figure 2.1, but for the mass flux spectrum over MSE vs. height for the full domain of the LES. The mass flux has been normalized by the 0.1 K MSE bin width and the domain area to give units of (g s^{-1} m^{-2} K^{-1}). The dot-dashed lines are the MSE of convective plumes with constant fractional entrainment rates of 50% km^{-1}, 20% km^{-1}, and 10% km^{-1} from left to right.

dot-dashed lines representing the MSE of convective plumes with constant fractional entrainment rates in Figure 2.2 reveals that the mass flux increases with height of the plume, before quickly falling off to zero as the plume approaches its nonbuoyancy level at the dashed $\overline{h^*}$ line. Note that much of the mass flux occurs at values of MSE associated with very diluted convective plumes, and very little is associated with the least diluted plume.

One of the advantages of this analysis is its ability to isolate mass flux due to diabatic processes in the simulation. Because MSE is approximately conserved for adiabatic processes, updraft and downdraft parts of an adiabatic perturbation will have similar values of MSE. Summing mass flux along a constant MSE (or in a narrow bin range) will cause these updrafts and downdrafts to cancel. For example, buoyant parcels rising in the simulation are a negative perturbation to the density field at a particular level. In the stable air surrounding the rising parcels, this perturbation propagates radially away in the horizontal as a gravity wave (Bretherton

and Smolarkiewicz, 1989). Even if the ascending branch of such a buoyancy oscillation were to experience condensation, it would still have the same MSE as the descending branch, as discussed in the previous section.

Figure 2.3 is an illustration of the strength of this effect. Since the simulation uses a periodic domain, at any level the domain averaged vertical velocity, and the net mass flux, will be zero. All the updrafts and downdrafts must cancel over the domain at each level to maintain mass continuity. A simple way to find the updraft mass flux is to find the sum of the vertical velocity w only over those points for which w > 0 (m s^{-1}). All of the ascending sections of any buoyancy oscillation are considered, but none of the corresponding descending sections. This leads to the large values for mass flux plotted as a dashed line in Figure 2.3. However, first summing all the mass flux for points with very similar MSE values (the MSE bins of Figure 2.2), and then summing over only the MSE bins with a net upward mass flux gives the smaller values of the solid line in Figure 2.3. This illustrates the large amount of mass flux

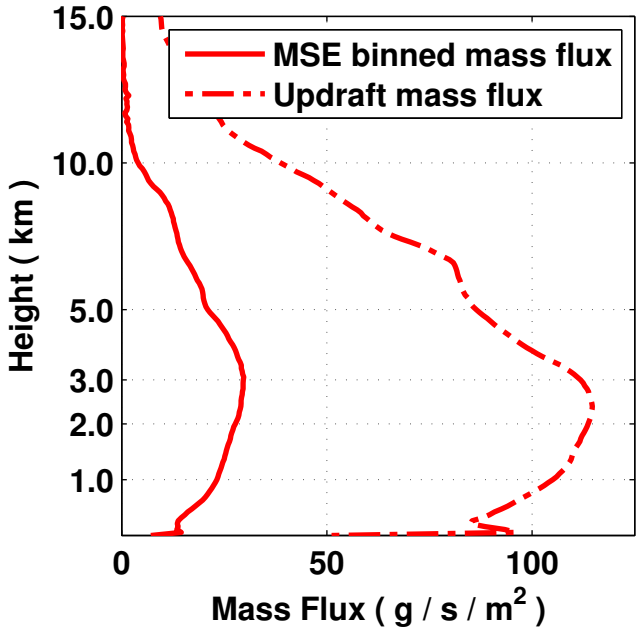

Figure 2.3. Mass flux found by summing over the MSE bins in Figure 2.2 which have positive mass flux (solid) and by summing all points in the simulation with positive mass flux (dashed).

potentially associated with buoyancy oscillations in the simulation, and the ability of the MSE spectral analysis to isolate the diabatic mass flux, that is, the transport occurring in response to the large-scale convective instability.

2.3 Vertical velocity and buoyancy

As discussed in the previous section, the mass flux in each MSE bin is found by summing the vertical velocity of all the points in the Giga-LES that have an MSE value in each bin range. In the AS74 cumulus parameterization, it is not necessary to resolve individual values of vertical velocity, only the mass flux of each cloud type that occurs in response to an instability. However, in more detailed cumulus parameterizations, the statistical distribution of vertical velocity is considered so that microphyiscal processes and the production of precipitation can be considered. One example is the cumulative distribution function (CDF) of vertical velocity used in the Donner (1993) parameterization.

With this in mind, I made a preliminary investigation of the statistical distribution of vertical velocity by finding the average vertical velocity in each MSE bin at each height, shown in Figure 2.4. While Figure 2.2 is a normalized measure of the mass flux and is readily comparable between simulations, Figure 2.4 illustrates particular values in the simulation and is not normalized. Note that the highest values of vertical velocity are associated with the points in the simulation that are the least dilute. There appears to be a consistent distribution of smaller values of vertical velocity for more and more dilution. The large section of green color in Figure 2.4 indicates that the average vertical velocity in this region of the MSE and height distribution is negative, but very close to zero. This is probably due to the great number of quiescent or gently subsiding points composing the unsaturated environment around the saturated updrafts.

One of the primary forces that acts to change the vertical velocity is the buoyancy. The thermal buoyancy B is defined in Equation (2.7) as the difference between

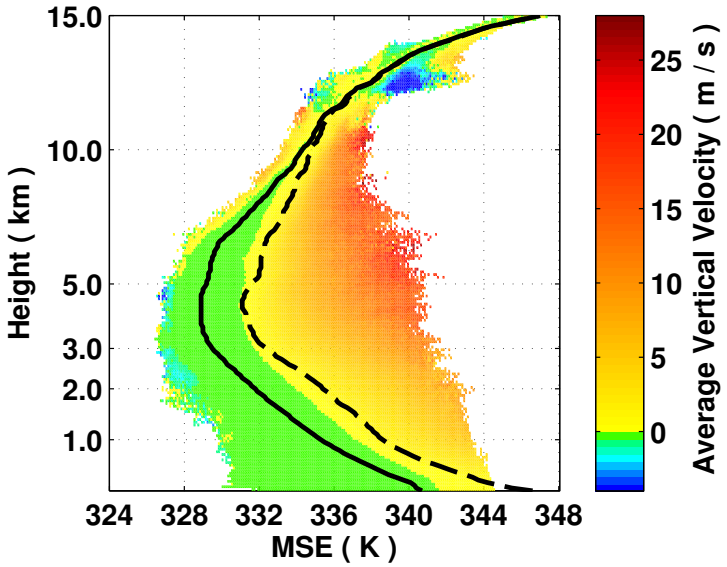

Figure 2.4. The average vertical velocity (m s^{-1}) in each MSE bin vs. height for the full domain of the LES.

the potential temperature θ of a grid point and the horizontally averaged potential temperature at that height, $\overline{\theta}$. To understand part of what determines the distribution of average vertical velocity shown in Figure 2.4, I have plotted the average thermal buoyancy in each MSE bin vs. height in Figure 2.5.

$$B = \frac{g}{\overline{\theta}}(\theta - \overline{\theta}) \tag{2.7}$$

Figure 2.5 shows positive buoyancy in the region to the right of the dashed saturation MSE line, consistent with the idea that that region is populated by cloudy buoyant updrafts. Much of the region with slightly negative average vertical velocity shown in green in Figure 2.4 has a positive average buoyancy. This is consistent with the idea that that region is populated by downdrafts being forced by other processes that overcome the positive buoyancy to produce subsidence, such as the pressure gradient force or weighting by condensate. Interestingly, there is a prominent but isolated region of negative average buoyancy at values of MSE higher than the domain average, but less than the saturation value of the domain average MSE, from about 3

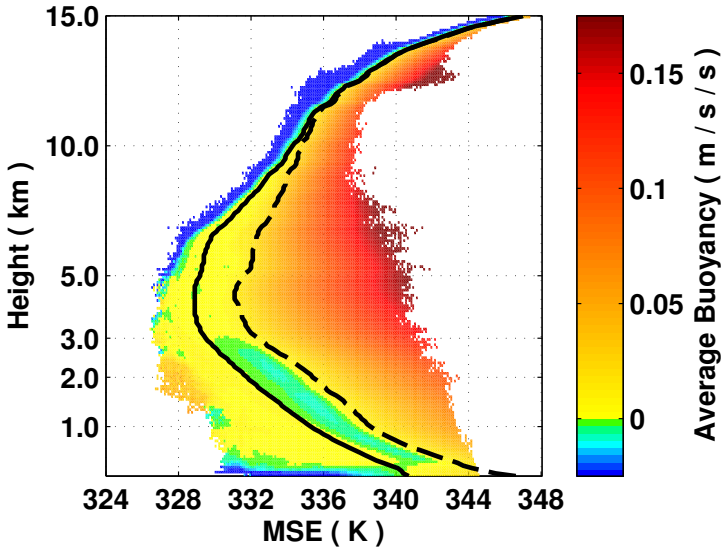

Figure 2.5. The average buoyancy (m s^{-2}) in each MSE bin vs. height for the full domain of the LES.

km height down to near the surface. Why is negative buoyancy confined to this region of MSE space? What processes contribute to the downdrafts that are occurring in MSE bins with negative average buoyancy versus bins with positive average buoyancy? An investigation of the microphysics and cloud condensate distribution in MSE space may shed light on these questions.

By plotting the average cloud condensate q_n from the simulation in the MSE bins of Figure 2.6, I reveal more of the nature of the points to the right of the black dashed $\overline{h}^*$ line. I have already shown that they represent a small fraction of 1% of the points in the simulation, and that they have large positive values of vertical velocity. Figure 2.6 shows that the average point in this MSE region contains a considerable amount of nonprecipitating cloud condensate.

The same analysis is performed for precipitating condensate as well (Figure 2.7). It shows that there is a considerable amount of precipitating condensate to the right of the black dashed $\overline{h}^*$ line. The distribution of these two types of condensate shows an interesting pattern. There is a bimodal distribution for average cloud condensate, with a maximum of more than 3 g kg^{-1} just below 3 km height an a similar maximum

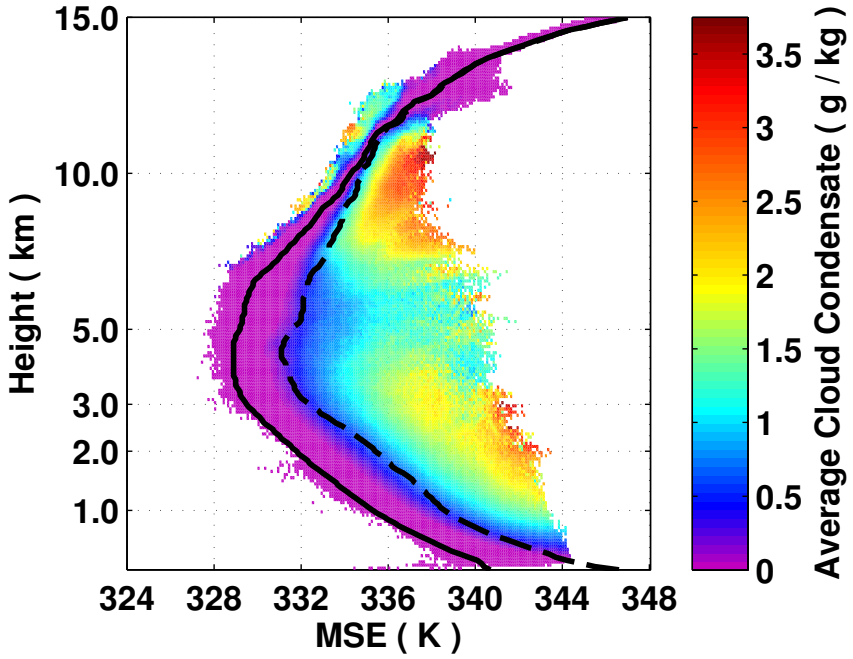

Figure 2.6. The average nonprecipitating cloud condensate (ice and liquid) mixing ratio (g kg^{-1}) in each MSE bin vs. height for the full domain of the LES.

near 10 km, both at some of the least diluted MSE points (Figure 2.6). Meanwhile, the average precipitating condensate mixing ratio has a single maximum in the region that is right between the maxima of the average cloud condensate, near 340 K and 5 km height.

Figure 2.2 is a normalized measure of the mass flux that is comparable to other simulations, like Kuang and Bretherton (2006), their Figure 11, which inspired it. It is the sum of a particular value in the simulation, the vertical velocity. A simulation with similar thermodynamic structure and forcing as the GigaLES would produce a similar mass flux summed over MSE bins, but the particular values of MSE bin average vertical velocity could conceivably be very different depending on the dynamics, entrainment, and mixing characteristics of the case.

The whole GigaLES domain can be thought of as representing what would be the subgrid scale of a single column over the tropical ocean in a global climate model (GCM) (Khairoutdinov et al., 2010). In a crude sense, the problem of parameterizing

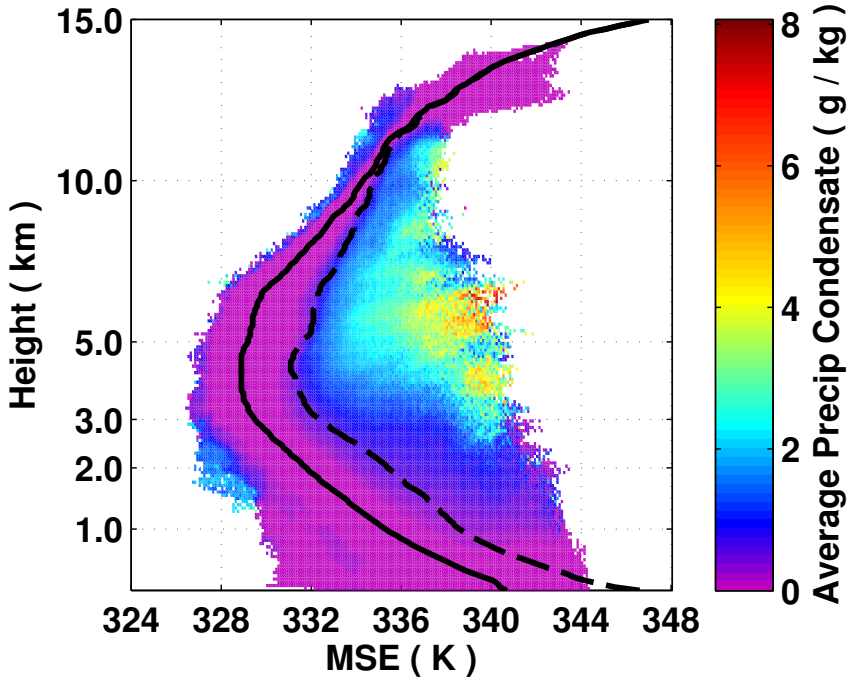

Figure 2.7. The average precipitating condensate (ice and liquid) mixing ratio (g kg^{-1}) in each MSE bin vs. height for the full domain of the LES.

the effects of the GigaLES cumulus convection for the GCM is like attempting to find the net mass flux distribution of Figure 2.2. Average cloud properties ultimately may not need to be resolved in a parameterization, only the total effects of the convection must be represented. Additionally, examining the total distribution of cloud properties such as mass flux, cloud condensate, and precipitating condensate over MSE and height is a way to investigate the properties of the convection in the simulation over the large domain without needing to consider individual clouds.

With this in mind, the total cloud condensate in the simulation by volume is plotted in Figure 2.8. The sum of the mixing ratios in each bin is multiplied by the air density to give the amount of condensate by volume, and then multiplied by the size of each grid volume to give the total amount of condensate in kg. Then, the value is normalized by the domain volume and the 0.1 K MSE bin width to give the units shown in Figure 2.8. It shows that over the full domain, most of the cloud condensate

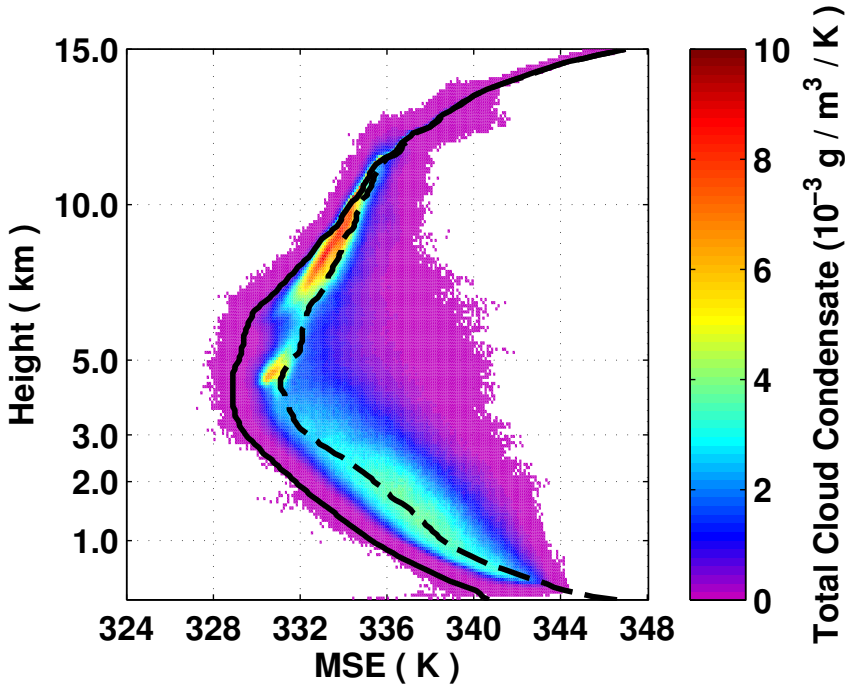

Figure 2.8. The spectrum of total nonprecipitating condensate (ice and liquid) by volume over the full domain. The condensate total has been normalized by the 0.1 K MSE bin width and the domain volume to give units of g m^{-3} K^{-1}.

is concentrated near the profile of saturated environmental MSE. This is in contrast to Figure 2.6, which showed large values for bin average cloud condensate at high values of MSE. Because of the frequency distribution in Figure 2.1, the preponderance of small values of bin average cloud condensate near $\overline{h}^*$ adds up to a much higher total amount of cloud condensate than the large bin average values could because of their rarity.

The same can be said for Figure 2.9, which is calculated as described above, but for the precipitating condensate. Unlike the cloud condensate, the precipitating condensate has a fall speed in the simulation, and the condensed precipitation quickly leaves the region where it formed. Thus, the maximum of the total precipitating condensate spectrum over MSE occurs near the $\overline{h}^*$ profile at upper levels and comes closer and closer to the environmental value of h at low levels.

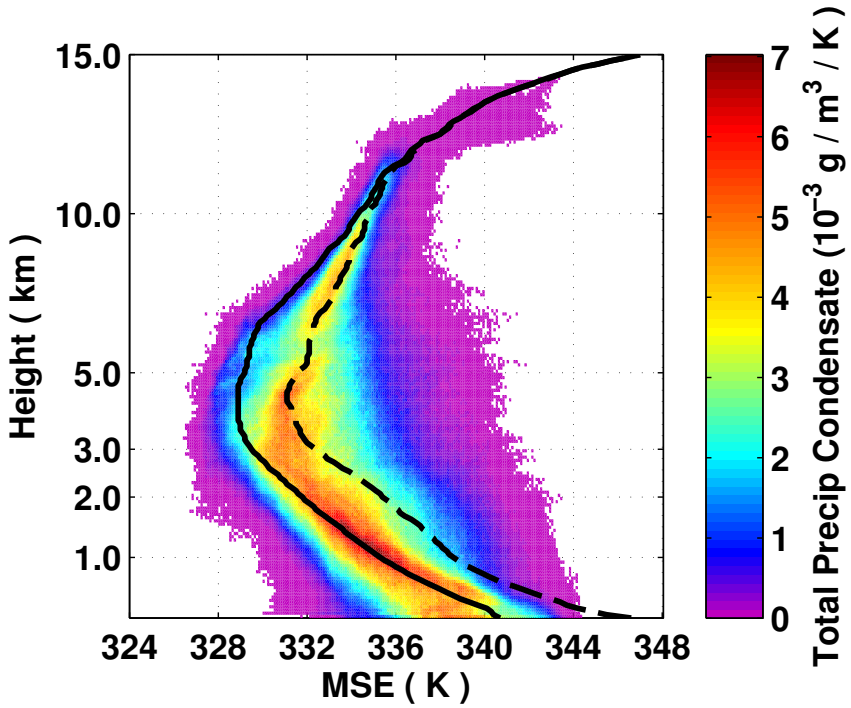

Figure 2.9. The spectrum of total precipitating condensate (ice and liquid) by volume over the full domain. The condensate total has been normalized by the 0.1 K MSE bin width and the domain volume to give units of g m^{-3} K^{-1}.

2.4 Cloudy updrafts and downdrafts

Since, as was discussed in the previous section, the MSE spectrum of net mass flux can be thought of as an example of what would need to be parameterized as the subgrid scale for a GCM, how much of that spectrum is due to cumulus updrafts? That question can be answered by finding the net mass flux in each bin as in Figure 2.2, but for a restricted threshold of points. I calculate the mass flux spectrum for Figure 2.10 by only considering those points in the domain with cloud condensate $q_n > 0$ (g kg^{-1}) and vertical velocity $w > 0$ (m s^{-1}). This restriction removes the ability of the technique to cancel out the fluxes from buoyancy oscillations because of the $w > 0$ (m s^{-1}) requirement. However, I note that the magnitude of the binned values is very similar for this figure and the region of Figure 2.2 to the right of the $\overline{h}^*$ profile. This suggests that the whole region in MSE space to the right of the $\overline{h}^*$ profile has positive vertical velocity. This is consistent with the idea that that MSE

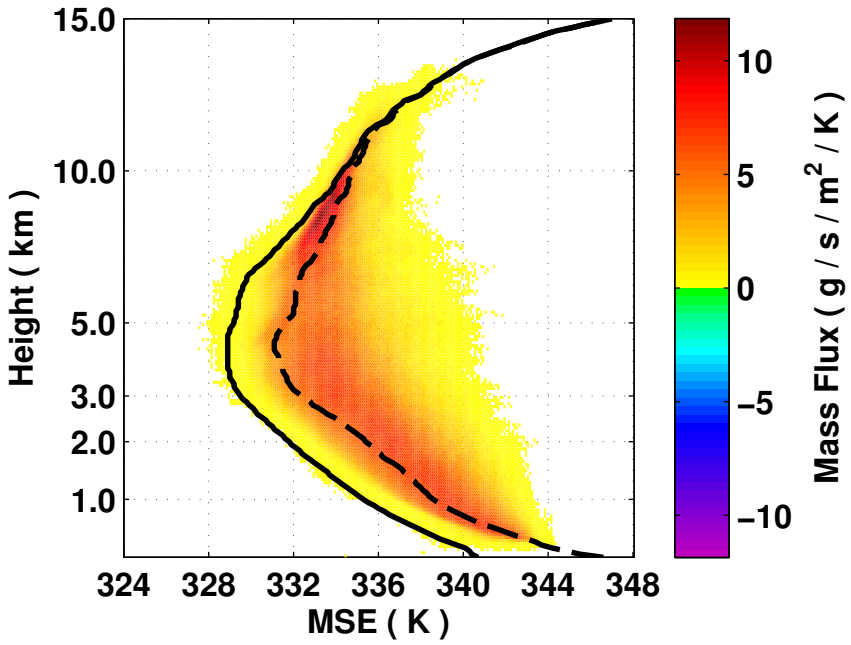

Figure 2.10. The mass flux spectrum as in Figure 2.2 but now only for points with cloud condensate $q_n > 0$ (g kg^{-1}) and vertical velocity $w > 0$ (m s^{-1}).

region is populated by cumulus updrafts.

The mass flux spectrum in cloudy downdrafts is very different. Figure 2.11 is calculated in the same way as Figure 2.10, but the domain is restricted to those points in the simulation for which cloud condensate $q_n > 0$ (g kg^{-1}) and vertical velocity $w < 0$ (m s^{-1}). This shows that most of the mass flux in cloudy downdrafts occurs just to the left of the $\overline{h}^*$ profile in MSE space. In contrast, Figure 2.12 shows the spectrum of mass flux for points with precipitating condensate $q_p > 0$ (g kg^{-1}), vertical velocity $w < 0$ (m s^{-1}), and relative humidity $q_v/q_v^* < 1$. These unsaturated precipitation containing downdrafts are concentrated around the environmental profile of $\overline{h}$. Another notable difference from Figure 2.11 is seen at the lowest values of MSE at low levels in Figure 2.12. There are almost no cloudy downdraft points in Figure 2.11 at all with MSE less than the domain average $\overline{h}$. Figure 2.12 shows that the existence of points with MSE as low as 332 K below 1 km is due at least in part to precipitation containing unsaturated downdrafts bringing low MSE air down from the

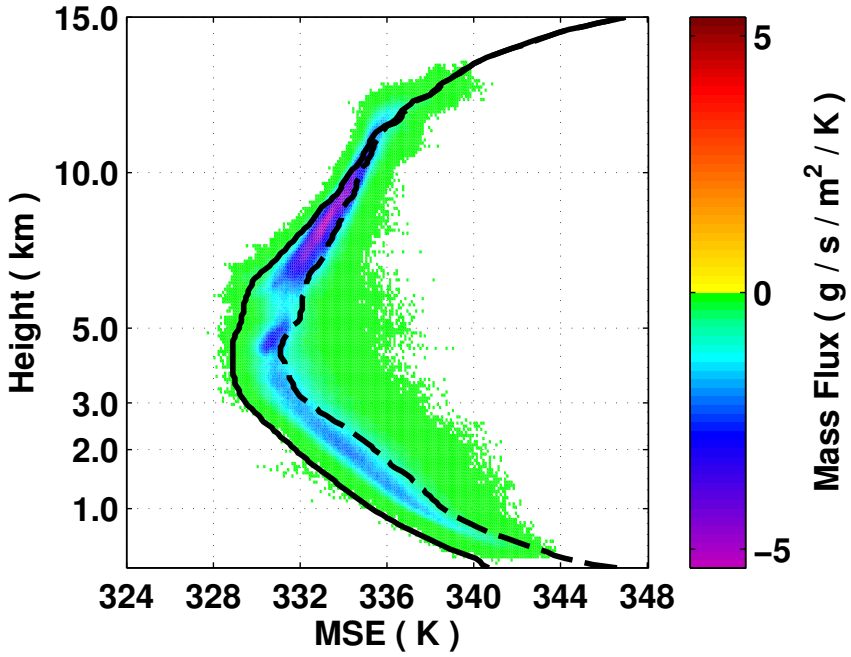

Figure 2.11. The mass flux spectrum as in Figure 2.2 but now only for points with cloud condensate $q_n > 0$ (g kg^{-1}) and vertical velocity $w < 0$ (m s^{-1}).

mid-levels.

If the region to the right of the $\overline{h}^*$ profile in the figures above is associated with cloudy updrafts, and the $\overline{h}$ profile is characteristic of the cloud free environment, is the region in-between the two associated with the near cloud environment? Not necessarily, but possibly. MSE mixes linearly, so intermediate values of MSE between two points could represent mixtures between the two. But it is possible that such values could just be realizations of the environmental variability. It is also possible that some real, unique properties of the set of values due to mixing between the cloud and the environment could be masked by a large number of points in the simulation that simply have a variability in MSE that overlaps the MSE of the points just outside the clouds. In the next chapter, I will apply the MSE spectral analysis to specifically selected regions of the simulation domain to overcome this uncertainty and understand more about the near-cloud environment.

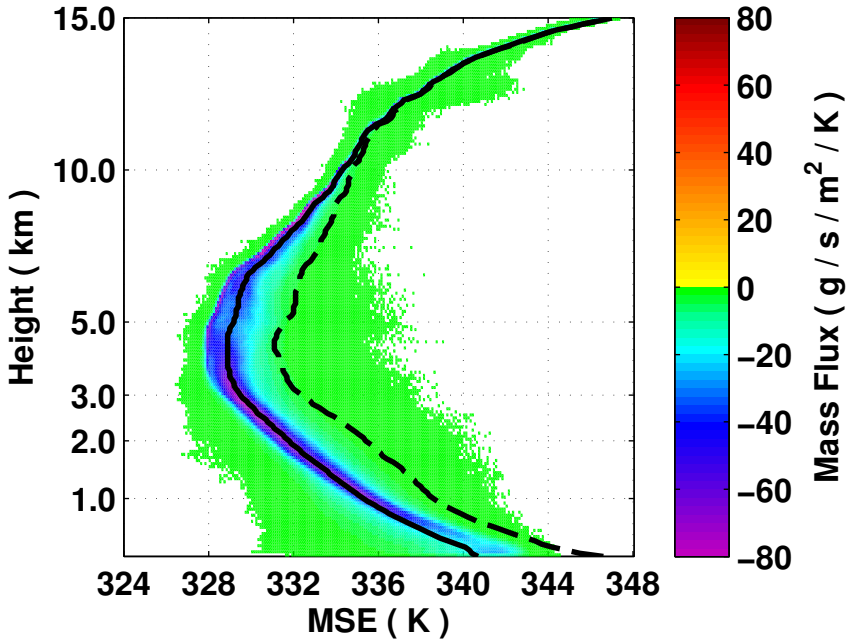

Figure 2.12. The mass flux spectrum as in Figure 2.2 but now only for points with precipitating condensate $q_p > 0$ (g kg^{-1}), vertical velocity $w < 0$ (m s^{-1}), and relative humidity $q_v/q_v^* < 1$.

CHAPTER 3

DOWNDRAFTS IN THE NEAR CLOUD ENVIRONMENT OF CONVECTIVE UPDRAFTS

3.1 Methods

We identified 3-D cloudy updrafts in the Giga-LES as contiguous points with vertical velocity $w > 1$ m s^{-1} and condensed cloud water and ice mixing ratio $q_n > 0.1$ g kg^{-1}. Contiguity is defined as "face-sharing" adjacent, so diagonal connections are ignored. Individual 3-D cloudy updrafts are the discrete volumes of such contiguous points. We define the NCE as the region enveloping the exterior of the cloudy updrafts, up to 500 m away from the nearest cloudy updraft edge. This 500 m distance should be far enough away from the cloudy updraft to capture a narrow subsiding shell like that in HJ08, which was 100 m thick for shallow cumulus. We applied this selection method to 13 different hourly snapshots of the full 3-D simulated volume taken after the convection had reached a steady state and thereby identified over $400,000$ cloudy updraft volumes (Figure 3.1).

The largest cloudy updraft identified has a volume of 10^{12} m^3. This volume is equivalent to a cube 10 km to a side, which is a good approximation to a large cumulonimbus cloud. The smallest identified cloudy updrafts are simply single grid points, which cannot be considered well-resolved clouds. Because the number of cloudy updrafts of a particular size is distributed approximately exponentially (Figure 3.1), the smallest cloudy updrafts make up the vast majority of those identified. We

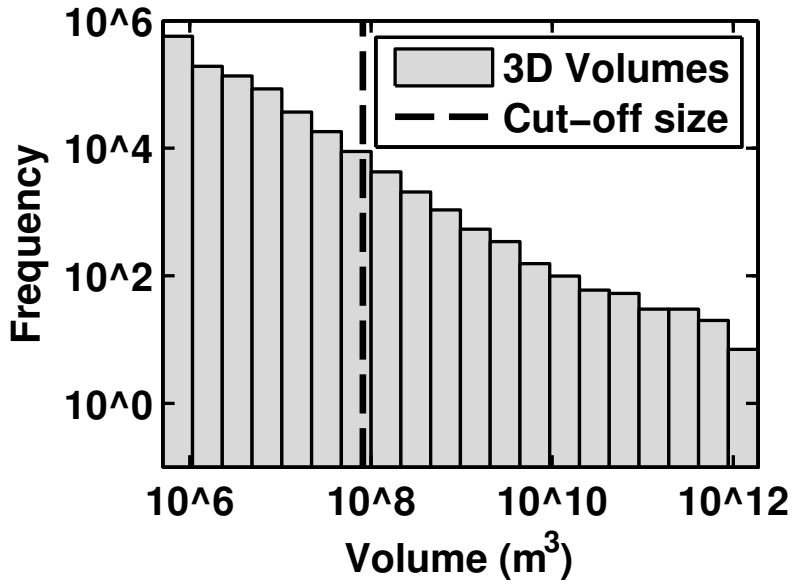

Figure 3.1. Log-log frequency distribution of cloudy updraft volumes. We ignore the group of volumes to the left of the dashed black line as they are composed of only a few model grid points. The cut off volume is that of a cube 450 m on each side.

therefore consider only the largest 10% of the cloudy updrafts to reduce the sample to those cloudy updrafts that are well-resolved. From this group of the largest volumes, the smallest has a size on the order of a 500 m$\times$ 500 m $\times$ 250 m volume, which may just barely represent a resolved feature. This truncation still leaves about $40,000$ resolved cloudy updraft volumes. For the remainder of the paper, the word "cloud" will be used to refer to a member of this group of the largest simulated 3-D cloudy updraft volumes.

We used two geometric statistics to take a closer look at the size characteristics of the clouds. A plot of the distribution of cloud vertical extent for different cloud base heights shows two distinct directions of variation (Figure 3.2). Almost all of the clouds with base heights at upper levels have small vertical extents (less than 2 km). In contrast, there are other clouds with vertical extents from a few hundred meters to nearly 14 km, but all have a cloud base at a height less than 1 km. This distribution is similar to what we would expect for a field of cumulus in different stages of their life cycles. Cumulus that will become deep towers begin to form near the surface in

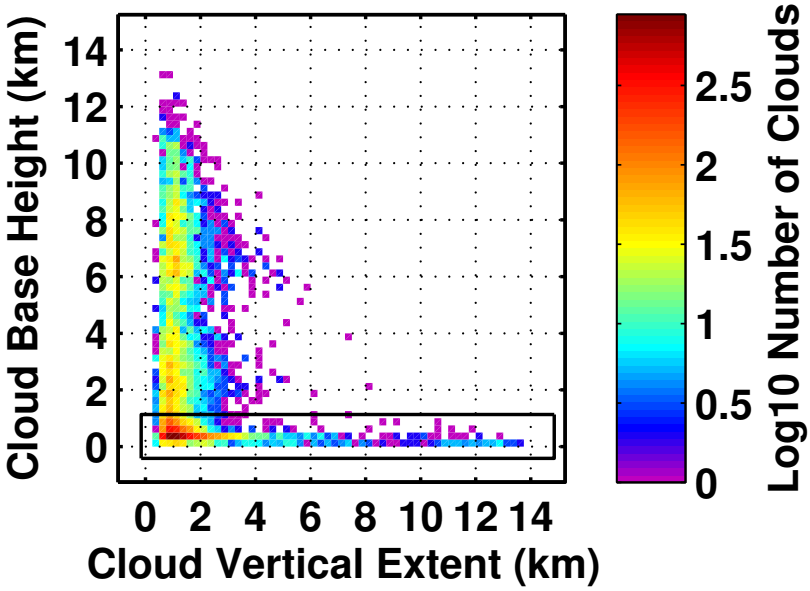

Figure 3.2. Frequency distribution of cloudy updrafts versus vertical extent and cloud base height. The group interpreted as growing and mature cumulus is outlined in the interior black box.

the mixed layer. They extend from low levels up to higher levels, eventually reaching a maximum height at their maturity. An active group of growing and mature cumulus would have a range of vertical extents and a cloud base near the surface, a distribution similar to the one shown in the interior black box of Figure 3.2. For clouds in the Giga-LES, we observe (not shown) that after reaching maturity, downdrafts and other processes eventually break the connection between the lower and upper levels of the cloud. This causes the height of the base of the updraft to increase as the cloud dissipates, and it eventually breaks into smaller pieces with little vertical extent. This is consistent with the conceptual picture of the life cycle of cumulonimbus (Ogura and Takahashi, 1971).

Interpreting the 3-D cloudy updrafts with low cloud bases as active growing and mature cumulus is also consistent with more recent research. In a detailed study of convective transport in a high-resolution CRM, Romps and Kuang (2011) measured the contribution to the mass flux at a particular height from eddies that originate

at other heights. They showed that a large majority of the air transported to the upper levels of their simulation by convection originates from within 200 m of the surface. Considering this, and our Figure 3.2, we restricted our sample to only those clouds which have base heights less than 1 km. We used this subset to study the characteristics of the NCE around developing and mature cumulus. We will refer to members of this subset as "active clouds" since we have removed the clouds that have the characteristics of dissipating cumulus from the analysis. Restricting our sample in this way allows us to study the processes occurring in the NCE of clouds that are dynamically similar, and actively transporting mass and moisture to upper levels.

To determine the role of mixing between the cloud and the far environment, we will examine the properties of the NCE in terms of an approximately conserved mixing variable. The moist static energy (MSE) in temperature units is $h = T + (g/c_p)z + (L/c_p)q_v$, as defined before. The MSE mixes linearly for all mixing processes, except those with phase changes that involve the latent heat of melting (Kuang and Bretherton, 2006). We counted the number of grid points that have similar MSE values at each height in the active clouds and their NCEs (Figure 3.3). We used a narrow bin range of $\Delta h = 0.1$ K, where we have expressed the MSE in units of Kelvins. In Figure 3.3, the solid black line represents $\overline{h}$, the MSE averaged horizontally over the entire domain. The dashed black line is the MSE that air with the domain average temperature would have if it were saturated. We refer to it as $\overline{h}^*$, defined as the horizontal average of $h^* = T + (g/c_p)z + (L/c_p)q_v^*$, where q_v^* is the saturation mixing ratio.

To see the distribution of a particular property, like the average value of buoyancy in each MSE bin, $\overline{B}$ (m s^{-2}), we find the average using the total number of points counted over either all clouds or their NCEs for each MSE bin. To reduce noise, we ignore any MSE bin that contains less than 1% of the maximum count found in a bin for that case.

The MSE values in the simulation can be used to infer the mixing history of

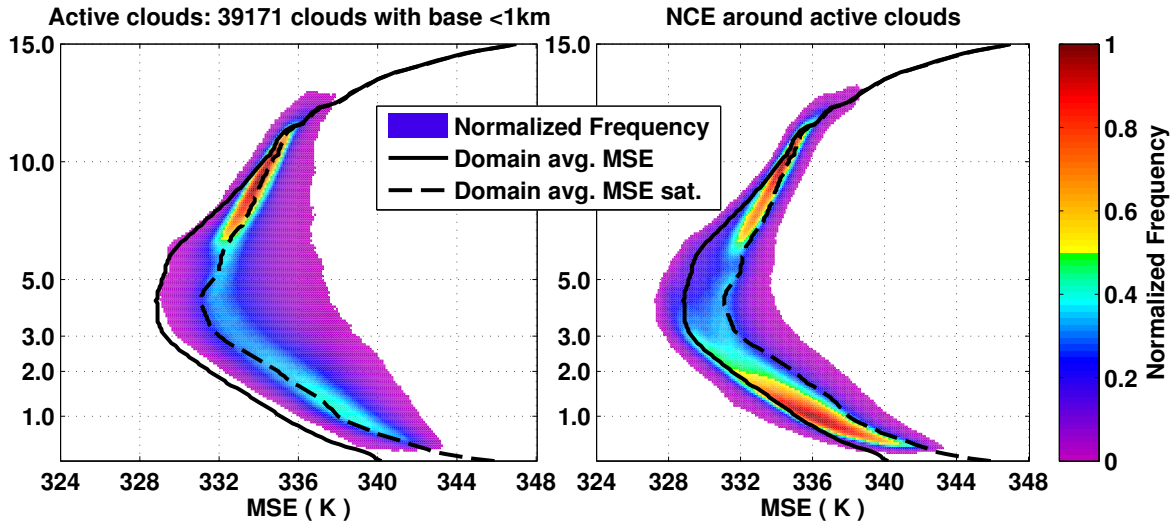

Figure 3.3. Moist static energy histograms showing the frequency of model grid points versus MSE and height for active clouds (left) which have a base < 1 km, and the NCEs around those clouds (right). The frequency is normalized by the maximum value for each region.

individual air parcels. Since MSE is conserved under saturated adiabatic and hydrostatic processes without melting or freezing, air rising from the boundary layer should have constant MSE unless it mixes with environment air and the MSE is reduced. Plotting the distribution of a variable versus MSE and height allows us to study the entrainment and mixing characteristics of this large simulation of convection. This method is based on Kuang and Bretherton (2006) and Khairoutdinov and Randall (2006), who have illustrated its usefulness. We used this technique to determine if mixtures between the cloud and the large-scale environment have the properties we would expect for a subsiding shell. We then calculate the net mass flux in the NCE and cloudy updraft regions. Our results build on the research of Heus et al. (2009) who validate a LES of compensating mass flux in subsiding shells against aircraft observations around shallow cumulus updrafts, and call for estimates to be made for the strength of this compensating subsiding shell mass flux for deep convective cases.

We expect the NCE region to contain many parcels with properties like those of the cloud since the NCE borders the cloudy updraft. We also expect the NCE to

contain many parcels with properties like those of the average large-scale environment. Because of the overall convex shape of the cloud boundary, the number of parcels in the NCE at a particular distance from the cloud boundary increases with distance, meaning many parcels are far from the cloud boundary and more likely to have average environment properties. Parcels in the NCE that have the properties of a subsiding shell will have a MSE between the cloud and average environment values, signifying mixing; and they must have negative vertical velocity and negative buoyancy as in HJ08.

3.2 Results

The plots of the distributions of MSE in the active clouds and their NCEs displays differences between the two regions (Figure 3.3). The maximum frequency in the NCE histogram is about twice as large as the maximum frequency in the active cloud histogram, but this is not shown since we normalized by the maximum frequency in each histogram to facilitate comparison. The plots show that the clouds contain some of the highest values of MSE, while their NCEs contain some of the lowest values of MSE. At low and mid-levels, the MSE in the NCEs is most frequent both near the $\overline{h}$ and the $\overline{h}^*$ lines, with a minimum in-between.

Air with MSE greater than $\overline{h}^*$ is buoyant with respect to the average environment (AS74). However, MSE alone does not determine whether air with MSE between $\overline{h}$ and $\overline{h}^*$ is buoyant. Plots of the average buoyancy in each MSE bin for each region are shown in Figure 3.4. Both the active clouds and their NCEs have negative average buoyancy in the region between $\overline{h}$ and $\overline{h}^*$. We refer to this region in MSE space as the "buoyancy sorting" region. We note that negative average buoyancy in the clouds decreases steadily with decreasing MSE in the buoyancy sorting region while below 5 km for the NCEs, the negative buoyancy decreases and then increases again.

To better understand this pattern, we performed a mixture fraction analysis for several pairs of cloud and environment parcels. A MSE spectrum plot of cloud

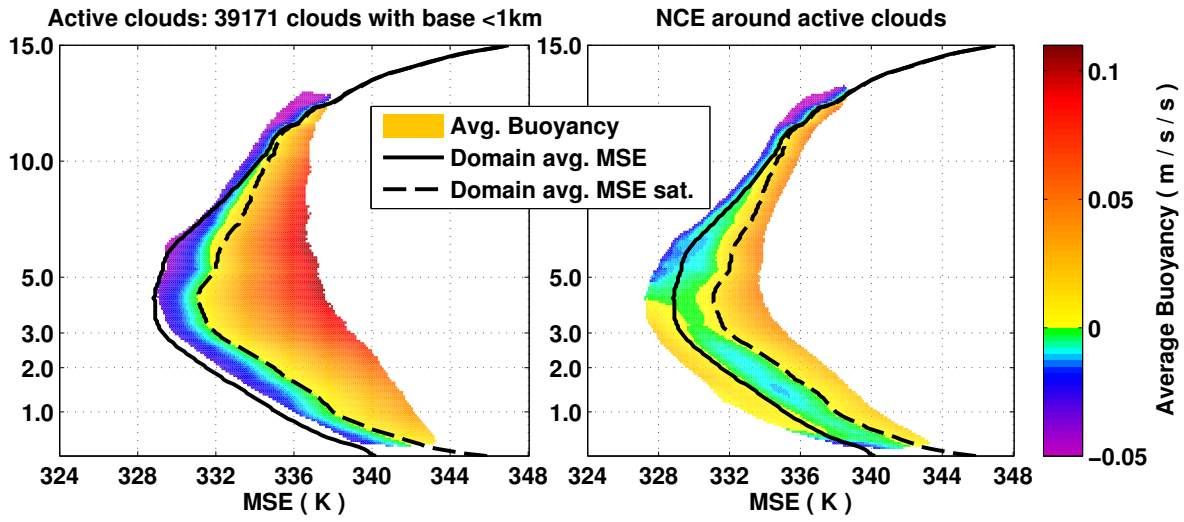

Figure 3.4. As in Figure 3.3, but now showing the average value of the buoyancy in each MSE bin for active clouds (left) which have a base < 1 km, and average buoyancy in each MSE bin in the NCEs around those clouds (right). The buoyancy is not loaded by the weight of condensate.

condensate q_n (not shown) displays increasing values of q_n as MSE increases at a given height in the clouds. We select MSE bin averaged values from 3 km height. In the 333 K bin for MSE, the average value of q_n in the clouds is 1 g kg^{-1}, in the 335 K bin q_n is 1.5 g kg^{-1}, and the 339 K MSE bin averaged q_n is 2 g kg^{-1}. We used these values to represent the properties of three different cloud parcels, and for an environment parcel we used the average environment values of 329 K for MSE and 0 g kg^{-1} for q_n. We calculated the buoyancy for different mixtures of the environment parcel and each cloud parcel in Figure 3.5.

We assumed that any cloud condensate q_n in the mixture will evaporate until either the mixture is saturated or the condensate is depleted; the resulting evaporative cooling reduces the buoyancy. In Figure 3.5, despite different initial values of MSE, mixtures between the environment and cloud parcels have minimum buoyancies near the same value of MSE in the buoyancy sorting region near 331 K. At this midpoint the mixtures deplete all of their available q_n to become just saturated. If, for example, the 339 K cloud parcel had a larger value of q_n like 3 g kg^{-1}, the minimum buoyancy

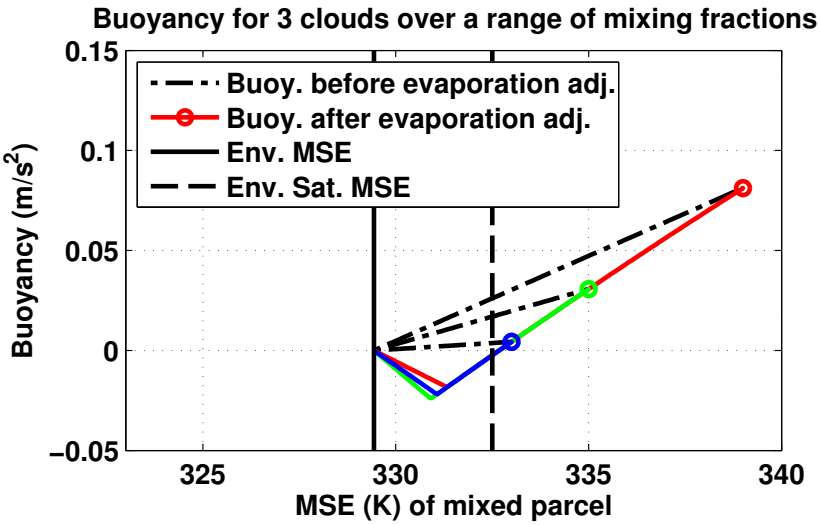

Figure 3.5. Buoyancy of mixtures of the average environment (solid black) and 3 idealized cloudy parcels. The cloud parcel properties are marked by red, blue, and green circles. Since MSE mixes linearly, it is a proxy for the mixing fraction between the environment and the cloudy parcels. Any condensate in a mixture is required to evaporate until either depleted or the mixture is saturated.

mixture would have a MSE closer to the environment since it would take a greater mixture fraction of environmental air to deplete the larger amount of condensate. Thus, the fact that the minimum buoyancy mixtures occur at the same value of MSE is due to the relatively constant proportional increase in the value of q_n with MSE in the cloud parcels.

We calculate a relative humidity for all points as q_v/q_v^*. Consistent with the "all or nothing" microphysics scheme of the simulation, the cloud parcels are necessarily saturated everywhere, including in the buoyancy sorting region. The distribution of the average relative humidity in the NCEs is displayed in Figure 3.6. The figure shows that the average relative humidity in the NCEs increases qucikly from the environmental average value of 85% to above 95% with increasing MSE from $\overline{h}$ to the middle of the buoyancy sorting region. Then, the MSE averaged relative humidity increases more slowly to 100% by the edge of the buoyancy sorting region at $\overline{h}^*$.

We next examined the properties of the NCEs by cloud type by splitting our sample of active clouds into three groups. Shallow clouds have cloud top heights less

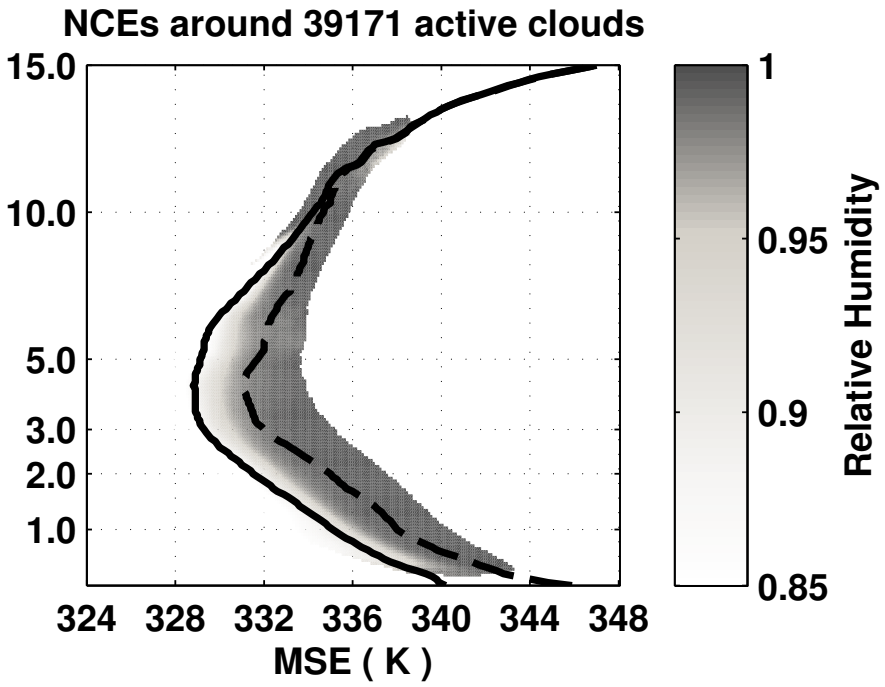

Figure 3.6. As in Figure 3.3, but now showing the average value of the relative humidity (q_v/q_v^*) in each MSE bin for active clouds (left) which have a base < 1 km, and average relative humidity in each MSE bin in the NCEs around those clouds (right). The scale has been truncated at the environmental average relative humidity of 85% for clarity. The thick black line is $\overline{h}$
and the dashed black line is $\overline{h}^*$.

than 3.5 km. The second group represents cumulus congestus clouds with tops from 3.5 km to at most 8.5 km. The final group consists of deep cumulonimbus clouds with tops higher than 8.5 km. The tallest in this group extend up to near 14 km, but most reach about 12 km. The MSE bin average vertical velocities versus MSE and z for the NCEs of the three different cloud groups are all very similar, broadly negative with a local minimum of -1 m s^{-1} in the buoyancy sorting region (not shown). We define and calculate a total mass flux for the NCEs of each cloud type group by multiplying the MSE binned average vertical velocity values by the total horizontal area of NCE points in each MSE and z bin and multiplying by the density. To ease comparison with other simulations, we then divided by the total area of the horizontal domain of the Giga-LES to give total mass flux in units of g s^{-1} m^{-2} (Figure 3.7).

This shows negative total mass flux in most MSE bins of the NCEs, with the

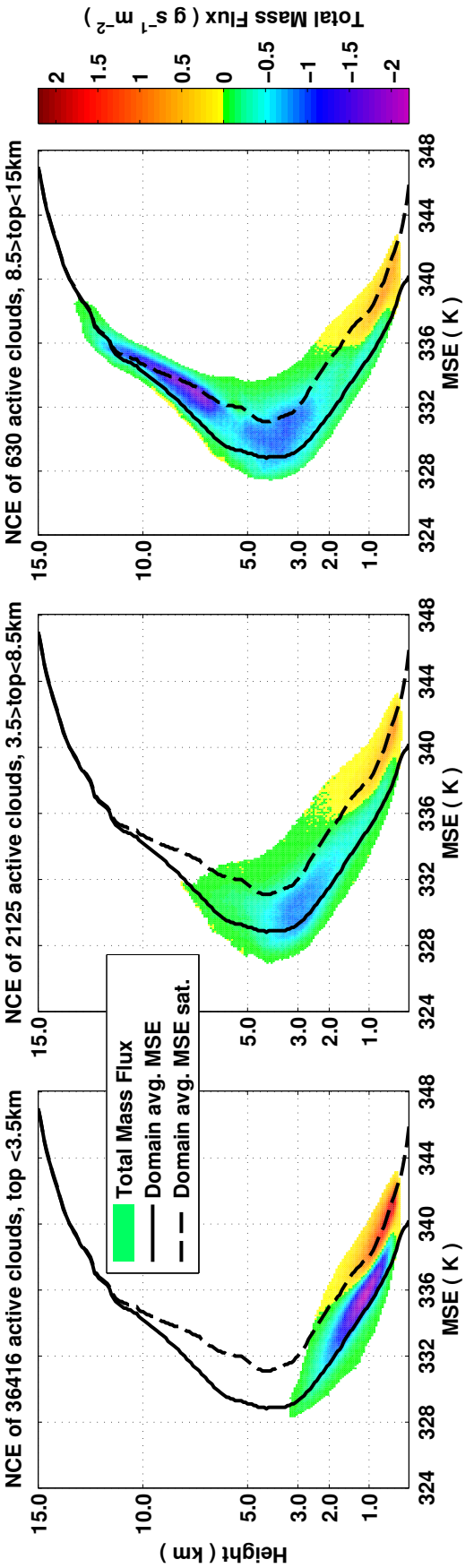

Figure 3.7. As in Figure 3.3, but now for the net mass flux in each MSE bin in all the NCEs around three distinct groups of active clouds. The net mass flux is found for the NCEs of all active clouds with a top height < 3.5 km (left), a top height between 3.5 km and 8.5 km (middle), and a top height between 8.5 km and 15 km (right).

largest negative values occurring in the buoyancy sorting region. Below 3 km, there are some positive total mass flux values at high values of MSE. These are cloud-like points that are part of the NCE due to just barely failing to meet the defined cloudy updraft threshold of $w > 1$ m s^{-1} and condensed cloud water and ice mixing ratio of $q_n > 0.1$ g kg^{-1}. The fact that such bins are not found at upper levels indicates that for deep clouds, outside of the defined cloudy updraft threshold, the NCEs are mostly composed of descending points. An estimate of the average vertical velocity can be implied by comparing Figure 3.7 with Figure 3.3.

We calculated total mass flux profiles for each group of NCEs by adding all the MSE binned values at each height. The same process is used to calculate total mass flux profiles for all the clouds in each cloud type group (Figure 3.8). At each level, the ratio of the total mass flux in the NCEs to the total mass flux in the clouds is a measure of the fraction of upward cloud mass flux that is compensated by subsidence in the NCEs. Heus et al. (2009) report this ratio as 48% for the descending shells around their LES shallow cumulus at a level of 1450 m.

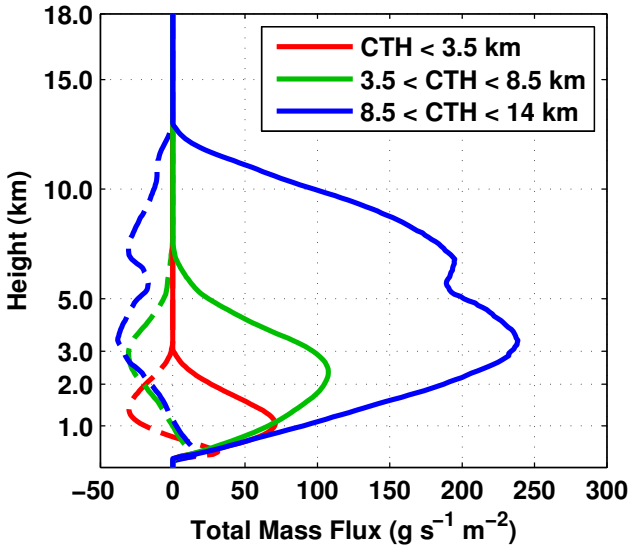

Figure 3.8. Profiles of net mass flux versus height for all NCEs (dashed) and active clouds (solid) with a top height < 3.5 km (red), a top height between 3.5 km and 8.5 km (green), and a top height between 8.5 km and 15 km (blue).

This compares favorably with our results, which show about 50% compensation at a similar level for our active shallow clouds. The cumulus congestus cloud type group has similar values of total mass flux in the NCEs but larger total mass flux in the clouds compared to the shallow cloud type group, giving a ratio of 25% at 2.5 km height. Similarly, the deep convection cloud type group has even larger values of total mass flux in the clouds while maintaining a similar negative net mass flux in the NCEs as the other groups, leading to a much lower net mass flux ratio of between 5% and 10% depending on the height.

Does this net mass flux in the NCE depend on the size of the defined NCE region? Recall that in Section 3.1, I define the NCE to be the region within 500 m horizontally of the edge of an active cloud, at each model level of the cloud. I assumed this NCE region would be large enough to contain any subsiding shell; indeed, I hoped it would be large enough to even include some points characteristic of the average environment. Because the MSE-based analysis effectively filters adiabatic motions, any quiescent rippling motions characteristic of the average environment that happen to fall into the NCE region will not contribute to the net mass flux. As long as the NCE region is large enough to contain the diabatic, evaporative-cooling driven subsiding shell, binning points by MSE should isolate the mass flux due to that diabatic process.

Increasing the size of the NCE further should not change the result significantly, because it will only include more points from the quiescent environment. To test this idea, the full analysis was repeated but with an NCE boundary 1000 m away from the edge of active clouds, and again with an NCE boundary at 1500 m. The result is shown in Figure 3.9. The net mass flux is found by summing all MSE binned points in each NCE region. It is clear that increasing the size of the NCE has increased the net negative mass flux at upper levels for the tallest clouds (blue lines) and decreased it for low clouds (red lines).

There are many possible explanations for this result. Speculating, one explanation involves the preponderance of small cloudy updrafts at low levels in the simulation.

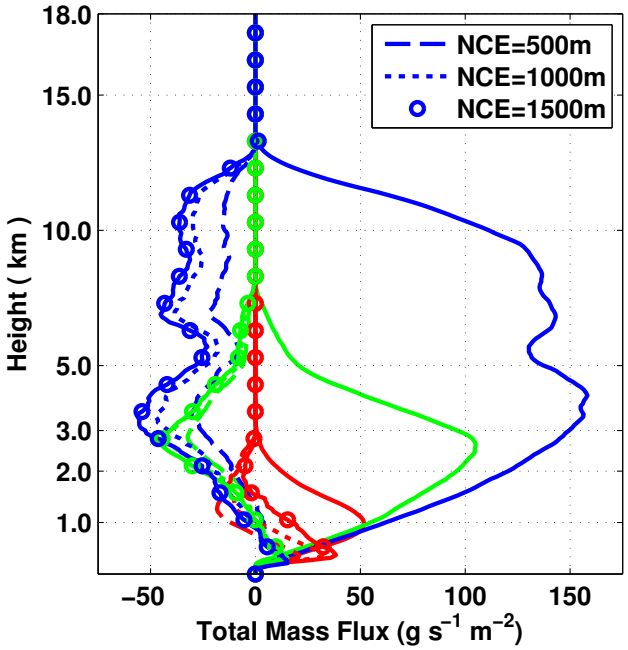

Figure 3.9. Profiles of net mass flux versus height for 500 m NCEs (dashed), 1 km NCEs (dotted), and 1.5 km NCEs (circles) around active clouds (solid) with a top height < 3.5 km (red), a top height between 3.5 km and 8.5 km (green), and a top height between 8.5 km and 15 km (blue).

Points outside of cloudy updrafts at low levels are more likely to have positive vertical velocity being in the vicinity of other cloudy updrafts. Fewer cloudy updrafts penetrate to higher levels, so points outside of cloudy updrafts at upper levels are more likely to contain downdrafts or be weakly subsiding. This could be why increasing the size of the NCE boundary increases negative net mass flux in the NCE at upper levels and decreases it at lower levels. In any case, it seems that increasing the NCE size has included points that significantly affect the net mass flux calculation.

Recall that the analysis in Section 3 showed that the region of MSE space greater than the environmental average MSE and less than the saturated environmental average MSE is the region where we would expect to see evidence of a subsiding shell. This MSE region, termed the "buoyancy sorting" region, contains mixtures between a cloud and its environment. The analysis for Figure 3.9 is repeated for Figure 3.10, but in this case, the mass flux is found not by summing all points in the

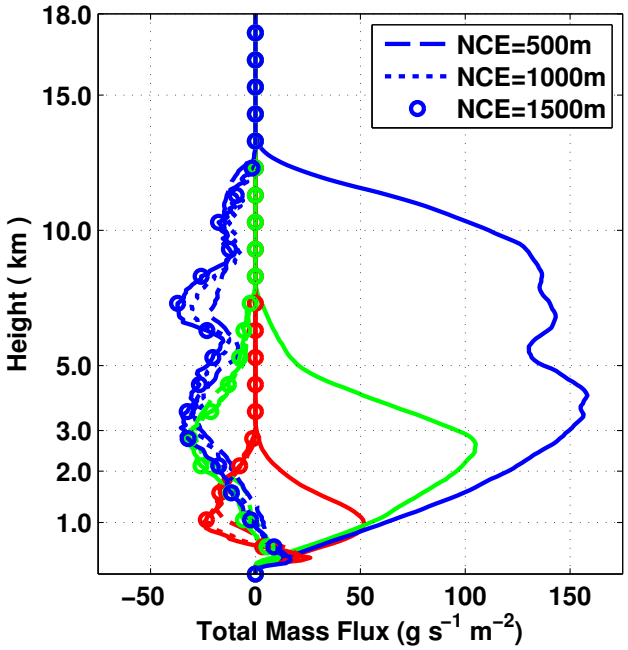

Figure 3.10. Profiles of net mass flux versus height as in Figure 3.9, but now calculated by summing MSE binned values only over the "buoyancy sorting" region of MSE space.

physical space of the NCE, but only those that fall into the buoyancy sorting region based on their MSE. Thus, Figure 3.10 shows that the buoyancy sorting region in MSE space defines and captures the mass flux associated with any subsiding shell in the NCE region.

CHAPTER 4

CLOUD CHARACTERISTICS

As discussed in Section 1.3, the work of Lin and Arakawa (1997a) clarifies how to physically interpret the individual convective plumes with constant fractional entrainment rates of the AS74 parameterization. They show that individual cloudy updrafts do not have the characteristics of convective plumes with constant fractional entrainment rates. However, within each individual cloudy updraft there are subcloud-scale elements that are experiencing entrainment and detrain from the updraft at different heights. Lin and Arakawa (1997a) find the subcloud elements from many different updrafts that are all detrained at the same height and group them to form a single "cloud type." They show that the properties of each cloud type can be well approximated by a convective plume with a constant fractional entrainment rate that reaches the same detrainment height. They leave several questions for future work. How are these subcloud-scale elements distributed throughout the cloud field? Is each individual cloudy updraft composed of a similar distribution of subcloud-scale elements? Is there a relationship between the distribution of different types of subcloud-scale elements in an individual cloudy updraft and the ultimate cloud top height (UCTH) of that cloudy updraft? Evidence that the answer to this question is "yes" would be encouraging for the "grey-zone" problem of parameterizing the effect of only a few cloudy updrafts over a relatively smaller horizontal domain (Dorrestijn et al., 2013). Evidence that the answer to this question is "no" would be encouraging for the development of stochastic parameterizations that consider individual cloudy updrafts to be statistical

samples of a "cloud spectrum" (Lin and Arakawa, 1997b).

4.1 Entraining convective plumes

To begin to answer these questions about the distribution of subcloud-scale elements with different rates of dilution leading to different detrainment levels in individual cloudy updrafts, I examine individual 3-D clouds in the Giga-LES and study the least diluted parcels within them. In Section 2.2, I derived Equation (2.6), which describes the change in MSE with height for a given fractional entrainment rate, λ. Because the equation is in differential form, λ can be either constant or variable with height. In the AS74 parameterization, individual convective plumes are assumed to have a constant fractional entrainment rate. In Lin and Arakawa (1997b), it is shown that each of these plumes is actually composed of subcloud-scale elements that reach the same top height as the plume. They show that the fractional entrainment rate of the subcloud-scale elements is variable with height, often larger at low levels followed by a reduced rate at upper levels. Does a 3-D cloud contain subcloud-scale elements diluted more or less than a convective plume with the same top height as the 3-D cloud? To answer this question and examine differences and similarities between 3-D clouds from the LES and entraining plumes, I will compare the MSE of individual 3-D clouds and the MSE of a plume modeled by integrating Equation (2.6) so that the plume reaches a nonbuoyancy level (NBL) at the cloud top height (CTH) of the 3-D cloud. This is done for three different clouds with top heights near 3 km, 5 km, and 10 km, respectively (Figure 4.1).

Figure 4.1 shows that the instantaneous composition of MSE in the simulated 3-D clouds has considerable internal variability that is not well described by a single entraining plume. The MSE of each convective plume (plotted in red) is almost everywhere close to the maximum MSE in each 3-D cloud at the same level. The plume MSE is far from the 3-D cloud average MSE (plotted dot-dashed), with the exception of the smallest cloud. The properties that result from solving the entraining

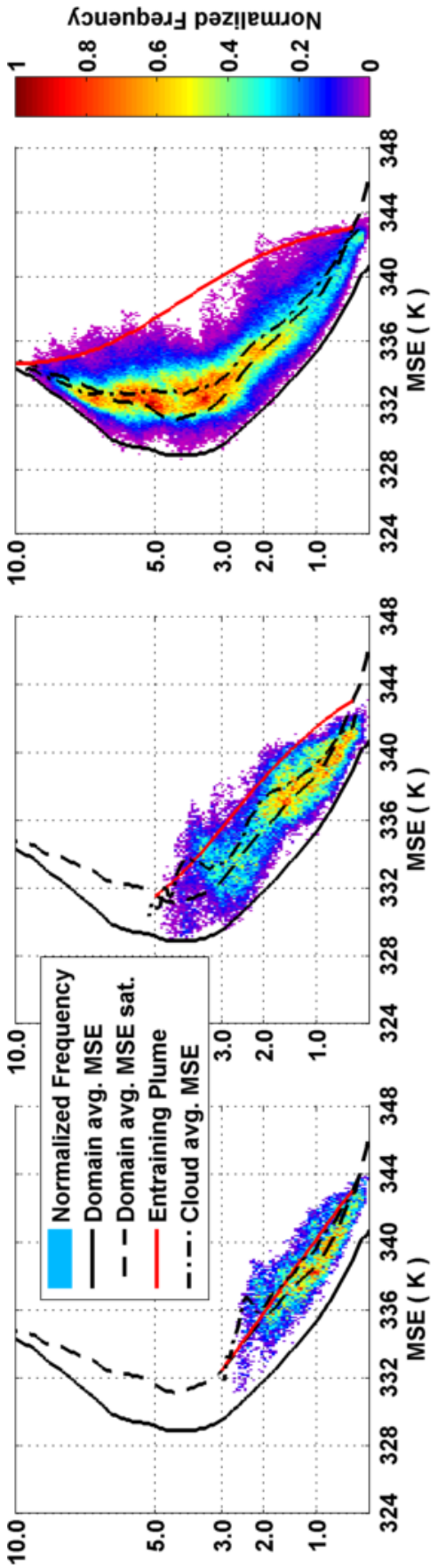

Figure 4.1. Frequency of MSE vs. altitude for three different instantaneous 3-D clouds. The domain average MSE and saturated MSE profiles are in black and dashed black, respectively. The dot dashed black line is $\overline{h_c}$, the mean MSE in the 3-D cloud. The solid red line is the MSE profile for an entraining plume with a NBL at the top height of each cloud, with λ =96% km^{-1}, 46% km^{-1}, and 13% km^{-1} for CTHs of 3 km, 5 km, and 10 km, respectively.

plume equation are supposed to represent the average properties of the plume. It seems that a large entrainment rate is required for the plume MSE profile to be near to the 3-D cloud average MSE profile, but that smaller entrainment rates are required to explain the range of observed CTHs. This method can simultaneously characterize the average MSE and the CTH of only the smallest 3-D clouds. This is similar to the problem found by Warner (1970) that the average liquid water content profile for a cloud and the correct cloud top height could not be simultaneously determined assuming a constant entrainment rate.

However, from the point of view of subcloud-scale elements, there is much in Figure 4.1 that is consistent with the ideas of Lin and Arakawa (1997b). The points in Figure 4.1 with maximum MSE at each height represent the least diluted subcloud-scale elements in each 3-D cloud. There is a notable gap in the mid-levels of the 10-km-tall cloud where the maximum MSE is less than the MSE of the convective plume with a corresponding 10-km height. Because the subcloud-scale elements may have variable entrainment rates, it is possible that a larger entrainment rate at low and mid-levels leads to higher dilution, followed by a reduced entrainment rate aloft that allows the subcloud elements to reach 10 km and define the top of the cloud. This would be consistent with the results of Lin and Arakawa (1997b), but without tracking the clouds and subcloud-scale elements through time, I cannot definitively make the same conclusion.

There are also some points in the 3-D cloud with MSE higher than the plume MSE at a particular height. Because the clouds in Figure 4.1 are instantaneous snapshots, they may contain subcloud elements that will rise even higher than the current CTH. To determine the height reached by the least diluted subcloud elements, the clouds must be tracked through time to determine their ultimate cloud top height (UCTH). Adding the dimension of time to this analysis is somewhat complex, and will be discussed in Section 4.3.

4.2 A simple parcel model

Before leaving the topic of the instantaneous cloud field and attempting to track clouds through time, I will attempt to examine the entrainment characteristics of the entire instantaneous cloud field instead of just three clouds as in Figure 4.1. I will present a method similar in simplicity to the one above for determining a λ to characterize the top height and entrainment characteristics of individual convective clouds. However, instead of the MSE of a plume, this method is based on the vertical velocity of a parcel. This choice is motivated by the greater spread in profiles of 3-D cloud average vertical velocity compared to profiles of 3-D cloud average MSE. Figure 4.2 shows these profiles for the seven different 3-D clouds whose CTH was near 5 km at the instantaneous time of 12 hours into the simulation. Because these clouds are at different points in their life cycles, some still growing, some mature, we expect to see differences in their properties. The greater spread in average vertical velocity profiles compared to average MSE profiles might allow greater resolution of the differences in dilution between clouds with the same CTH.

We can use a parcel model to calculate a parcel's vertical velocity as it moves

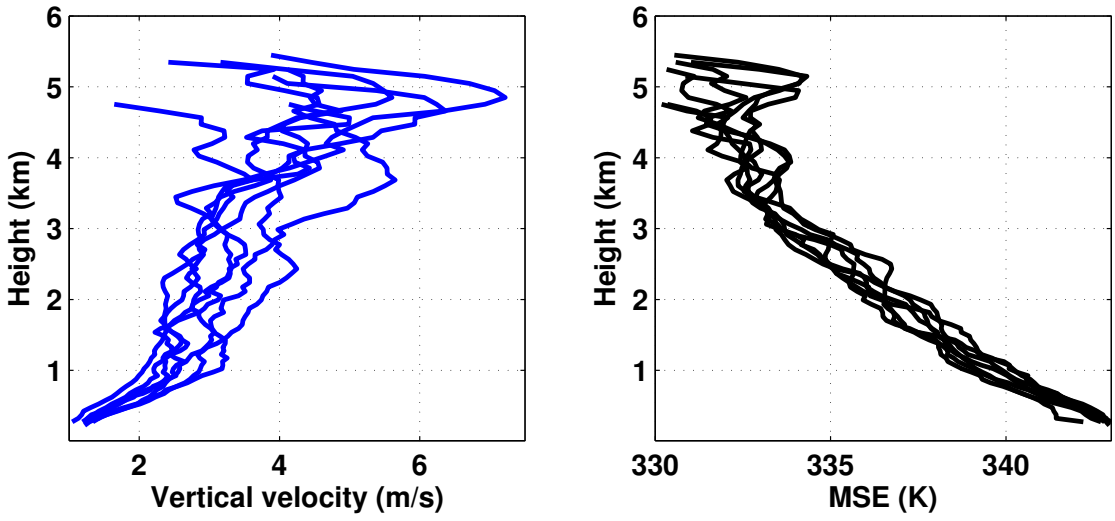

Figure 4.2. Profiles of average vertical velocity (left) and average MSE (right) for the seven clouds with a CTH near 5 km at the time of 12 hours into the Giga-LES.

over time, and consider a cloud at any instant to be composed of a collection of these parcels at different stages in their life. I will show that this vertical velocity-based method can characterize both the average vertical velocity in the 3-D clouds and their CTH, unlike the MSE-based method. This method will then allow study of how the distribution of subcloud-scale elements varies between different 3-D clouds. In particular, to be an improvement over the MSE-based method, it should illustrate a distribution of different entrainment rates among clouds with the same CTH.

By combining the continuity equation with the equation of motion and the 1st law of thermodynamics, after Holton (1992), the vertical velocity of a rising parcel is

$$\frac{dw}{dt} = -c_p\overline{\theta_v}\frac{\partial \pi_1}{\partial z} + \frac{g}{\overline{\theta_v}}(\theta(1 + \epsilon q_v - q_n - q_p) - \overline{\theta_v}) + D_w, \tag{4.1}$$

where $\overline{\theta_v}$ is the virtual potential temperature, π_1 is a perturbation of the nondimensional pressure, and q_v, q_n, and q_p are the mixing ratios of water vapor, cloud condensate, and precipitating condensate, respectively, in the parcel (Holton, 1992; S. K. Krueger, personal communication). D_w represents the tendency of w due to turbulent mixing. Substituting $w = dz/dt$ in Equation (4.1) converts the time derivatives to height derivatives,

$$\frac{dw}{dt} = w\frac{dw}{dz} = \frac{1}{2}\frac{dw^2}{dz}. \tag{4.2}$$

which gives the vertical gradient of the vertical kinetic energy. In analogy to Equation (2.6), I model the entrainment using "bulk" values of kinetic energy w_p^2 for the parcels and w_e^2 for the environment. In this case, "bulk" does not necessarily mean "average" but simply that one single value is used to represent the "bulk" of the most important aspects of the true distribution of values.

$$D_w = -\lambda_w(w_p^2 - w_e^2). \tag{4.3}$$

Assuming the vertical velocity in the environment is negligible, substituting (4.3) into (4.1) gives

$$\frac{1}{2}\frac{dw_p^2}{dz} = P + B - \lambda_w w_p^2, \tag{4.4}$$

where I have replaced the vertical perturbation pressure gradient acceleration term with P and the condensate-loaded buoyancy term with B. A vertical gradient in pressure perturbation can be caused by the movement of a parcel; this is called form drag, and it acts to reduce the vertical velocity. Such a gradient is also caused simply by gradients in buoyancy whether the parcel is moving or not. These effects are represented by decreasing the buoyancy by a factor a and increasing the strength of the fractional entrainment rate λ_w by a constant factor b:

$$\frac{1}{2}\frac{dw_p^2}{dz} = aB - b\lambda_w w_p^2 \tag{4.5}$$

The values $a = 1$ and $b = 2$ have been shown to be reasonable choices by de Roode and Bretherton (2003).

Instead of solving for a height varying λ_w for each cloud, I attempt to find a constant fractional entrainment rate λ_w that characterizes the dilution and CTH of each convective updraft in an analogy with Section 4.1. This is done by iteratively solving Equation (4.5) using the 3-D cloud average condensate loaded buoyancy profile $\overline{B_c}$ taken directly from the simulation while varying λ_w until a best-fit is found between the parcel model w_p and the cloud average vertical velocity profile $\overline{w_c}$. Curiously, the fit is only very good when the weighting of precipitation is ignored, so q_p is assumed to be zero in Equation (4.1). The best-fit is defined as the profile of parcel vertical velocity that minimizes the sum of squared deviations from $\overline{w_c}$.

It seems that this formulation can characterize both the mean vertical velocity in the cloud and the CTH to some extent, so the comparison between an instantaneous cloud mean profile and a simple model involving a constant fractional entrainment rate may be slightly better than Figure 4.1 would have led me to believe. There is some question as to whether this method should find the best-fit of the parcel w_p^2 to either $\overline{w_c}^2$ or $\overline{w_c^2}$. The left-hand side of Equation (4.5) represents the tendency of the parcel's mean vertical kinetic energy with height. But this method involves taking the square root and finding the best-fit of parcel vertical velocity w_p to $\overline{w_c}$. So why

not use the 3-D cloud average vertical kinetic energy $\overline{w_c^2}$ for the best-fit instead? The answer seems to be that it will not make much of a difference. Figure 4.3 shows these properties for the same 3 different height clouds as plotted previously. It shows the cloud average vertical kinetic energy (black), the cloud average vertical velocity squared (blue), and the parcel model w_p^2 (red), which was best-fit to the cloud average vertical velocity while varying λ_w through iterations of Equation (4.5). Note that the height scale varies. It is clear that while the error is largest for the tallest cloud, the differences between $\overline{w_c}^2$ and $\overline{w_c^2}$ are small compared to their differences from the parcel model values.

Is it valid to determine a characteristic constant λ_w for a single cloudy updraft by minimizing the difference between the parcel model result of integrating (4.5) and the cloud mean vertical velocity, instead of the cloud mean vertical kinetic energy? Certainly a more physically-based method would be to compare the average 3-D cloud vertical kinetic energy with the parcel vertical kinetic energy. An even more physically-based method would use a fractional entrainment rate that varies with height instead of being constant. Recent research like that of Romps (2010) shows that 3-D cloudy updrafts actually have a wide variety of entrainment rates at different levels instantaneously.

However, the motivation for this method is not to have the most physically accurate characterization of entrainment for an individual cloudy updraft; great advances have already been made in that regard (Romps, 2010; Dawe and Austin, 2011). The motivation discussed at the beginning of this section made clear that the intent of this method is to roughly characterize the rate of dilution and cloud top height for all the individual cloudy updrafts in the simulation so the range of variability from cloud to cloud may be revealed. The relevant question is, do all clouds with the same CTH have similar distributions of minimally diluted subcloud-scale elements?

To this end, I apply the method of finding a w_p profile for a parcel model best-fit to the $\overline{w_c}$ profile from a 3-D cloud to all "active" 3-D cloudy updrafts in the Giga-LES

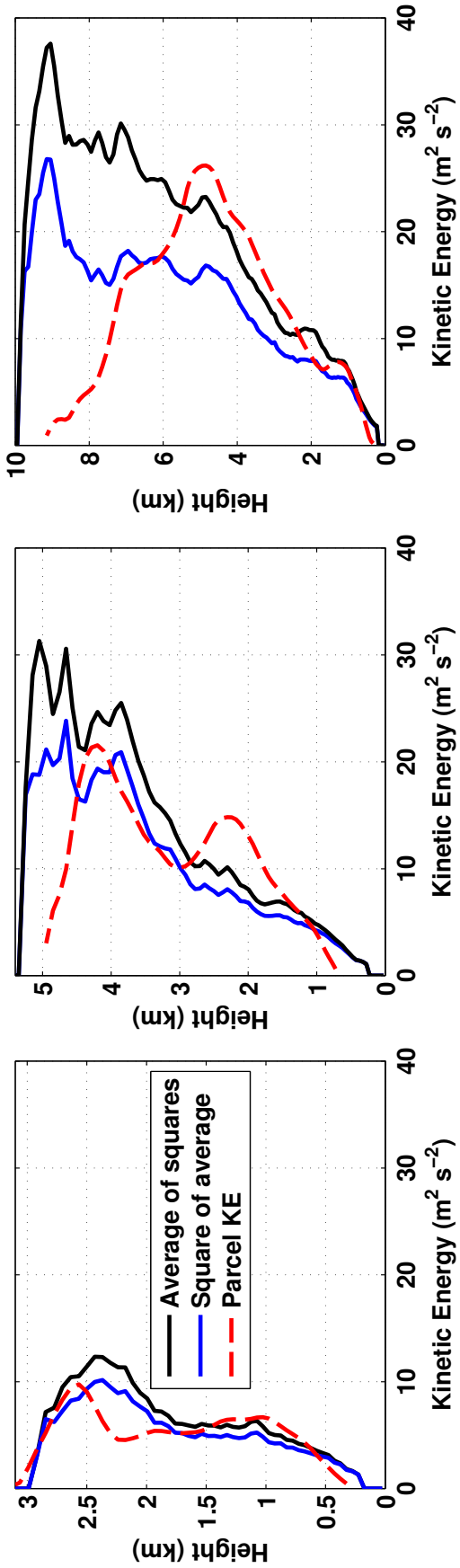

Figure 4.3. The 3-D cloud average vertical kinetic energy (black), the cloud average vertical velocity squared (blue), and the parcel model w_p^2 (red) for the same three clouds from Figure 4.1 with CTHs of 3 km, 5 km, and 10 km from left to right.

(as defined in Section 3.1). In Figure 4.4, I plot the characteristic constant fractional entrainment rate λ_w associated with each best-fit parcel profile.

Figure 4.4 can be used to illustrate possible cases for the ensemble properties of the convection. It will be helpful to interpret the variability displayed along horizontal and vertical transects of the figure. Along a line of constant bulk fractional entrainment rate λ_w, there is a distribution of clouds of different CTHs, up to a maximum value that appears to be a function of λ_w and CTH. This can be interpreted as a population of clouds with $\overline{w_c}$ and $\overline{B_c}$ profiles all characteristic of the particular λ_w. In the extreme case where λ_w will be constant throughout the cloud's lifetime, the highest observed CTH for a particular λ_w will represent the ultimate cloud top height (UCTH) for a particular cloud "type" λ_w. Similarly, along a line of constant CTH in Figure 4.4, there is a distribution of clouds with different λ_w. In the extreme case where λ_w uniquely determines UCTH, the distribution of clouds over different CTHs represents that they are in different stages of their life cycle, and those with the smallest λ_w

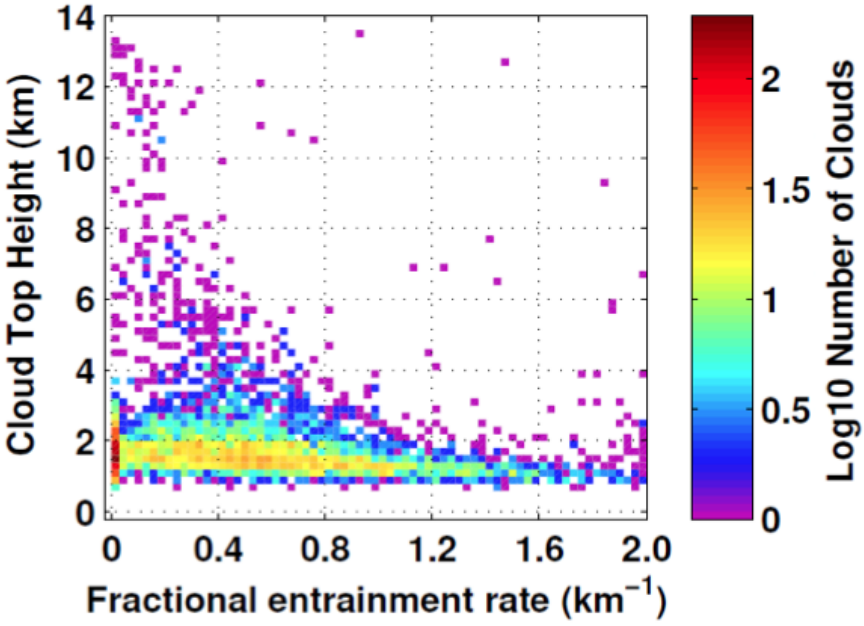

Figure 4.4. Frequency of occurrence of the characteristic bulk fractional entrainment rate λ_w vs cloud top height for all 3-D clouds from a instantaneous snapshot of the full Giga-LES domain.

could still be rising to a higher UCTH.

Figure 4.5 shows that the large difference ("error") between the best-fit vertical velocity profile and the $\overline{w_c}$ for many clouds with a low CTH is insignificant because they represent a relatively small amount of mass flux. This is illustrated by the distance of these points from the mass-flux-weighted average error profile. Figure 4.5 also shows that the difference between the parcel model and cloud average vertical velocity is on average about plus or minus 1 to 2 m/s over each 100 m level in the simulation. It is notable that this difference increases only slightly with height, less than the magnitude of the vertical velocity itself increases with CTH as seen in Figure 4.3. This method illustrates the variability of the distribution of minimally diluted subcloud elements for clouds with different and similar CTH levels. It illustrates that there is large variability in the population of diluted subcloud elements for clouds with a CTH at low levels, and minimal variability for clouds with a CTH at upper levels (Figure 4.4).

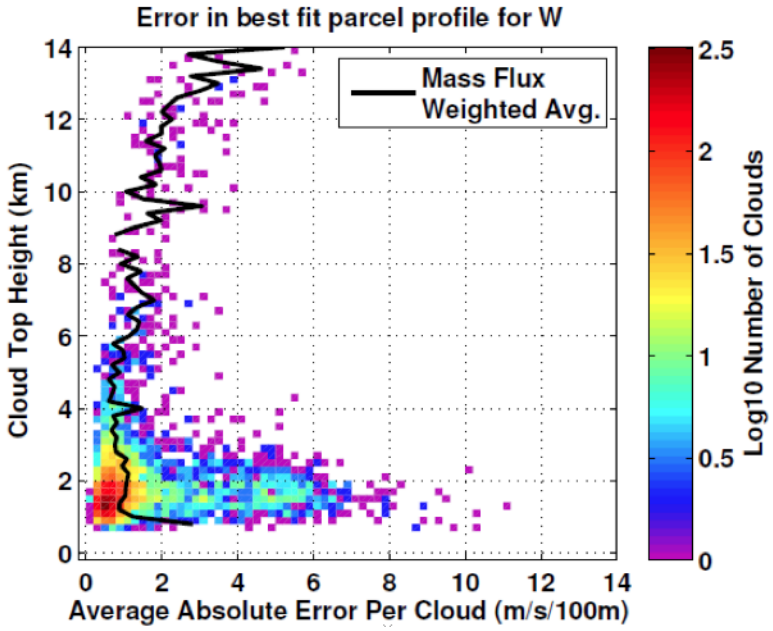

Figure 4.5. Frequency of occurrence of average absolute difference ("error") between a best-fit w_p profile and the $\overline{w_c}$ for each 3-D cloud from a instantaneous snapshot of the full Giga-LES domain. The mass flux weighted average error is plotted in solid black.

4.3 4-Dimensional cloud clusters

The above section concerning 3-D clouds was able to illustrate some of the insights and shortcomings that come from comparing instantaneous 3-D clouds to steady state entraining plumes. The problem is poorly posed. Because the 3-D clouds are instantaneous snapshots, it is not known what the UCTH of the cloud will be. The UCTH of a cloudy updraft is the highest level of detrainment for any subcloud element in the cloudy updraft. One way to investigate the distribution of subcloud elements over the population of individual cloudy updrafts is to track the subcloud elements individually and find the levels that they detrain from the cloudy updraft, as was done by Lin and Arakawa (1997b). Another method would be to track the cloudy updrafts individually and find the UCTH for each cloudy updraft. In that case, the detrainment level for all the subcloud elements would not be known, but the detrainment level of the least diluted subcloud elements would be known; it is by definition the UCTH of the cloudy updraft.

To understand the mass flux and MSE distribution in cloudy updrafts over time, an appropriate definition for the cloudy updrafts might simply be some threshold for mixing ratio of cloud condensate. The threshold should be chosen to represent an amount of cloudiness just visible to the eye to explain what a person would see as a distribution of cloud top heights. However, I have already discussed the probable existence of a distinct structural feature of descending air at the edge of a cloud called the subsiding shell in Section 3.2. It seems that the total cloudy mass flux is largely composed of two parts: the positive updraft mass flux of the active updraft and the evaporative cooling-driven subsiding shell mass flux. To isolate the cloudy updrafts, I continue to define a 3-D cloud as a contiguous region of grid points with cloud condensate mixing ratio greater than 0.1 g/kg and vertical velocity greater than 1 m/s, as discussed in Section 3.1.

To determine the ultimate cloud top height, I devise a method to connect 3-D cloudy updrafts through time. Using 3-D fields sampled at 5-minute intervals, if any

grid point of a contiguous 3-D cloud occupies the same location as any grid point of a contiguous 3-D cloud in the field 5 minutes later, they are connected as a 4-D object. This is done over the whole domain for 13 different samples spaced 5 minutes apart from hour 12 to hour 13 in the simulation. This process yields about 200000 different 4-D clouds. At any given time, a 4-D cloud may actually be composed of multiple 3-D clouds that either were connected in the past or will be in the future. For this reason, the more descriptive term "4-D cloud cluster" will be used as well as "4-D cloud" to refer to individual clusters of these spatially co-located groups of clouds. Each 4-D cloud is composed of multiple 3-D clouds that are connected over time. Sometimes, one 3-D part of the 4-D cloud is growing while another is dissipating, or vice versa.

I would like to see if these 4-D structures actually resemble the life cycles of known convective cloud types. I will begin by looking at the lowest cloud base height of the 4-D cloud and define a 4-D vertical extent as the distance between the lowest cloud base height and the highest cloud top height achieved at any time. Figure 4.6 shows

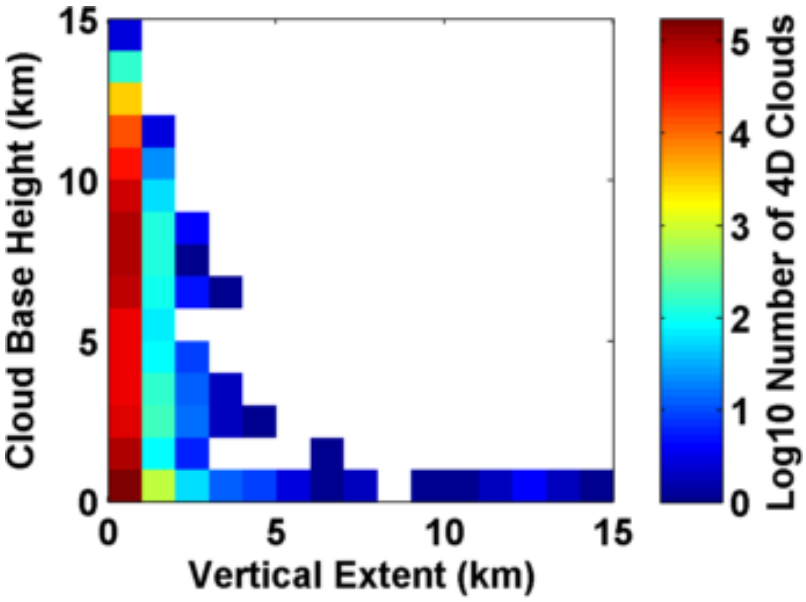

Figure 4.6. Frequency of occurence of 4-D cloud clusters over different lowest cloud base heights and vertical extent. The vertical extent is defined over time such that the maximum cloud top height may occur at a different time than the lowest cloud base height.

the frequency distribution of 4-D clouds for various values of the lowest cloud base height and the vertical extent. Just like with the 3-D clouds, we see a large number of clouds over all cloud base heights having a small vertical extent of 1 to 2 km. Most notably, the upper right corner of the figure is empty. This is because all the clouds with large vertical extents have a low cloud base height. This is a good sign that the 4-D connection method was able to capture the full life cycle of several deep convective clouds.

In an analogy with Section 3.1, we redefine a 4-D cloud as an "active" cloudy updraft such that it has, at any time over the chosen hour of simulation, a cloud base at a height of less than 1 km. So we exclude from this group the vast majority of clouds because they have small vertical extents and high cloud base heights. Within the group, there is a nonlinear distribution of ultimate cloud top heights. There are 11 4-D clouds with a highest cloud top height of over 10 km. There are 8 different 4-D clouds with cloud top heights between 5 km and 10 km, and 857 with top heights between 1 km and 5 km. Most of these lowest clouds have UCTHs less than 2 km; there are only 169 4-D clouds with top heights between 2 km and 5 km.

I expect that each 4-D cloud cluster will contain some points diluted very little by mixing. If I have captured most of the life cycle of the cluster, I would not expect to see any points diluted so little as I would expect for a plume with an entrainment rate such that it reaches a height higher than the 4-D clouds ultimate top height. Such a case would imply that the convective cluster's kinetic energy had not fully dissipated and it may still reach some higher UCTH. This is illustrated further in Figure 4.7.

In Figure 4.7, the MSE distribution summed over time is shown for the entirety of three different active 4-D cloud clusters with UCTHs near 3km, 5km, and 10km from left to right. These 4-D clouds are not related to and do not contain the 3-D clouds plotted in Figure 4.1, although they appear similar. I also plot the MSE of an entraining plume with a NBL at the UCTH of the 4-D cloud determined from (2.6) in red. Compared to the 10 km high 3-D cloud in Figure 4.1, the tallest 4-D cloud

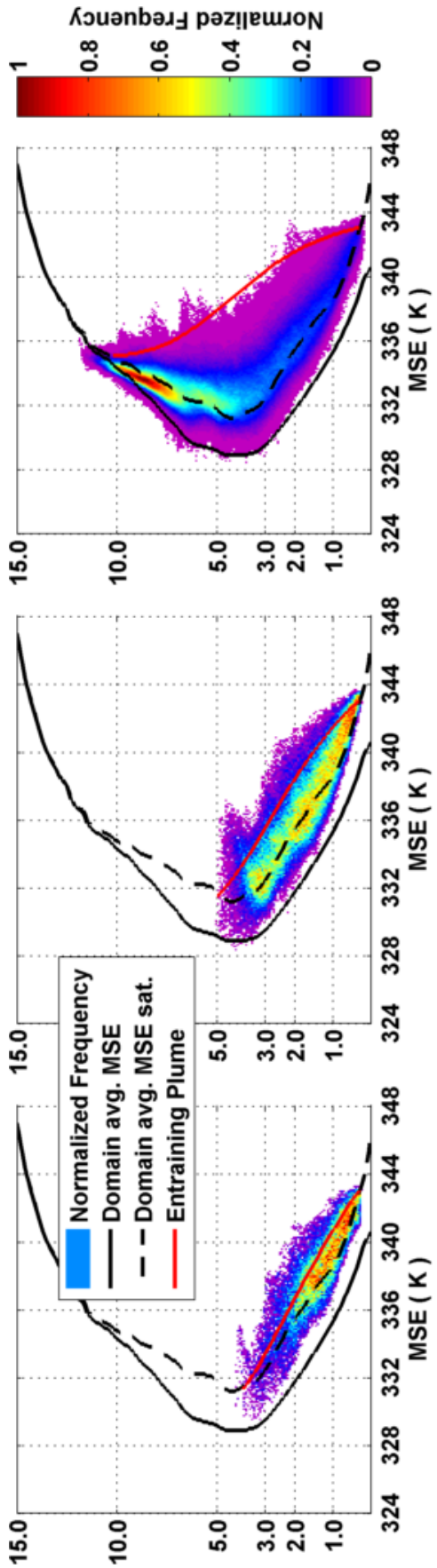

Figure 4.7. As in Figure 4.1, but now for 4-D cloud clusters. In red, I plot the MSE for an entraining plume with the same NBL as the UCTH for each 4-D cloud. The constant bulk fractional entrainment rate λ_h =0.74 km^{-1}, 0.45 km^{-1}, and 0.12 km^{-1} for CTHs of 3 km, 5 km, and 10 km, respectively.

cluster has maximum MSE much more similar to the MSE of an entraining plume with the same top height. The gap in the mid-levels of the right-most panel of Figure 4.1 is not present in the right most-panel of Figure 4.7. Looking at all three panels of Figure 4.7, you can also see that at a particular low level like 2 km, the maximum value of MSE observed increases from shallower to deeper 4-D cloud clusters. This is evidence that I am capturing the life cycle of the convection in the 4-D cloud clusters.

However, the two shallower 4-D cloud clusters with top heights near 3 km and 5 km contain many points less diluted than the convective plume that matches the UCTH of the 4-D cloud. It is possible this method could be too connective. For example, at the start of the analysis time, a dissipating bit of cumulus congestus could have moved over a shallower cumulus humilis, giving the appearance of an ultimate cloud top height being reached. It is possible to imagine all sorts of coincidences of cloud in the simulation that could lead to various cloud top height variation with time. Since there is some uncertainty, I will examine the vertical profile of horizontal area of different 4-D cloud clusters over time (Figure 4.8). The 4-D clouds displayed in Figure 4.8 are the same as those displayed in Figure 4.7.

Figure 4.8 shows some reasonable structure for the 4-D clouds. The level of maximum cloud horizontal area rises over time indicative of normal cloud growth, ruling out the chance that a strange coincidence of cloud overlap produced the pattern of CTH over time. However, very little of the dissipation stage of the 4-D cloud with an UCTH near 3 km is captured. Similarly, very little of the initiation stage of the 5 km UCTH 4-D cloud is captured. Only the 4-D cloud with an UCTH near 10 km has had both its growth and dissipation captured by the method. It seems that an hour is enough time to capture the growth and dissipation of a cumulus cluster, but only if the cluster's lifetime happens to be centered on the chosen hour of interest. The right hand panel of Figure 4.8 bears a striking resemblance to some of the figures shown in the study of the life cycle of numerically simulated convection of Ogura and Takahashi (1971).

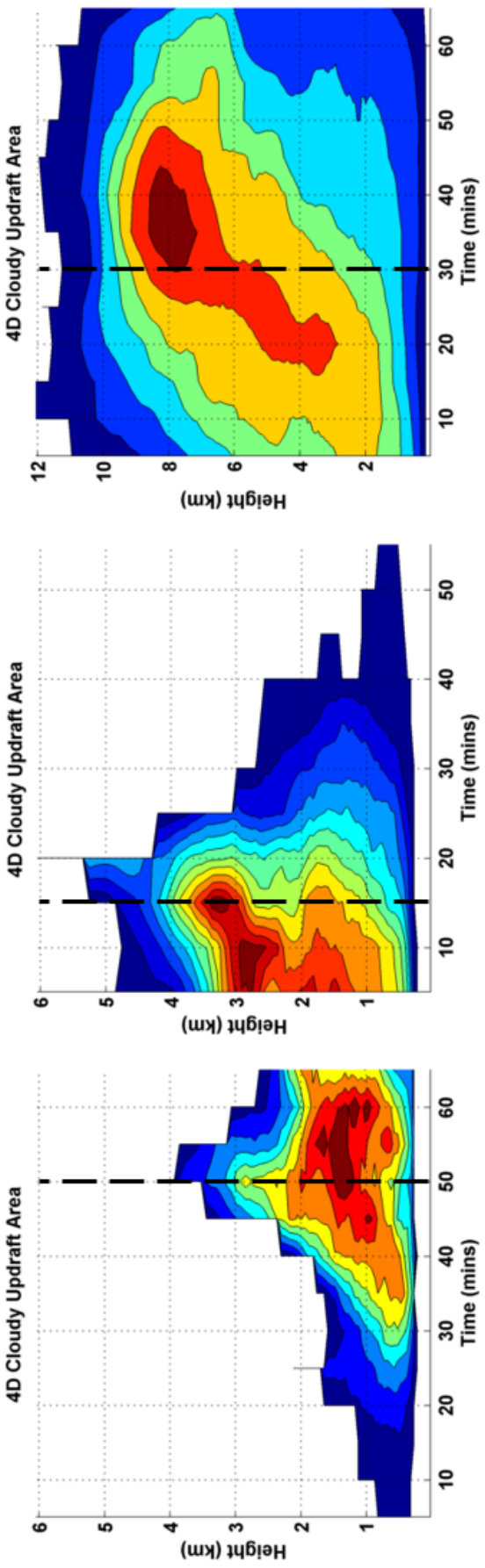

Figure 4.8. The horizontal area of 3 different 4-D clouds over height and time, normalized by the maximum area over the time frame for each 4-D cloud. A vertical dashed black line is included to denote the subjectively determined "maturity" time for each 4-D cloud.

By subjectively defining a "maturity time" for each 4-D cloud in Figure 4.8, I can make a version of Figure 4.4 but for individual times over the 4-D cloud life cycle. All the 3-D clouds that compose the 4-D cloud at a single time frame are summed together and treated as a single "3-D subensemble" of the 4-D cloud cluster. The average buoyancy $\overline{B_c}$ profile for each 3-D subensemble at each time is used while iterating through characteristic λ_w values until the parcel vertical velocity profile w_p from Equation (4.5) is best-fit to the average vertical velocity $\overline{w_c}$ profile. When the different characteristic λ_w values are compared against the different CTHs of the subensembles, any consistent evolution over time through the space of the two variables will be revealed. Evolution over time in the horizontal or vertical directions on the plot can be explained in different ways as discussed at the end of Section 4.2.

Figures 4.9, 4.10, and 4.11 show some sign of evolution of the 3-D subensembles in both the horizontal and vertical directions on each plot. For Figure 4.9, this evolution could be interpreted as an increasing CTH over time for a somewhat varying but

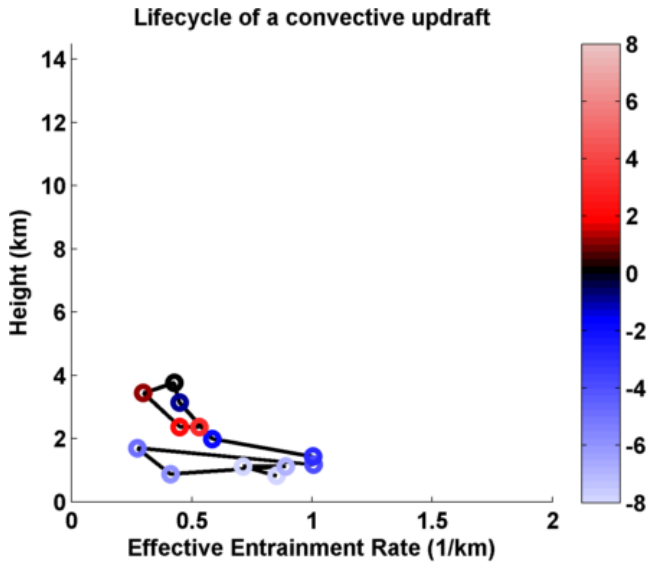

Figure 4.9. As in Figure 4.4, but now for the characteristic λ_w vs CTH for the 3-D subensembles over time for the 4-D cloud illustrated on the LHS of Figure 4.8. Cooler and warmer colors respectively denote the amount of time before and after the subjectively determined "maturity" time in units of 5-minute timeframes. Black represents the "maturity" time for the 4-D cloud.

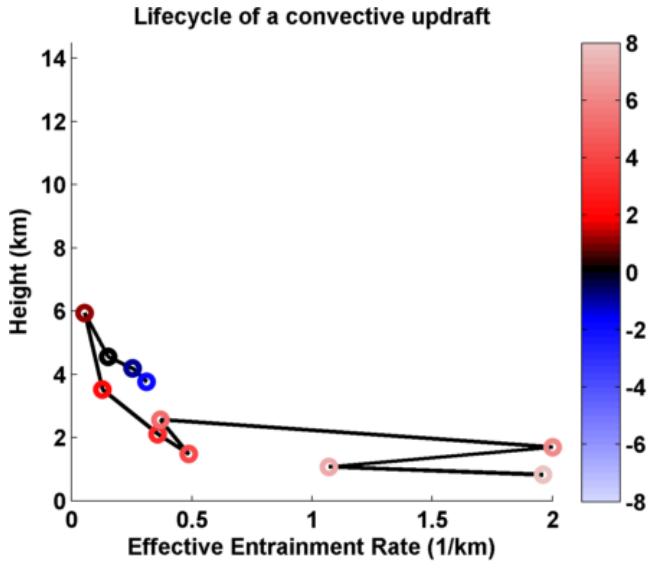

Figure 4.10. As in Figure 4.9, but now for the characteristic λ_w vs CTH for the 3-D subensembles over time for the 4-D cloud illustrated on in the middle of Figure 4.8. Cooler and warmer colors respectively denote the amount of time before and after the subjectively determined "maturity" time in units of 5-minute timeframes. Black represents the "maturity" time for the 4-D cloud.

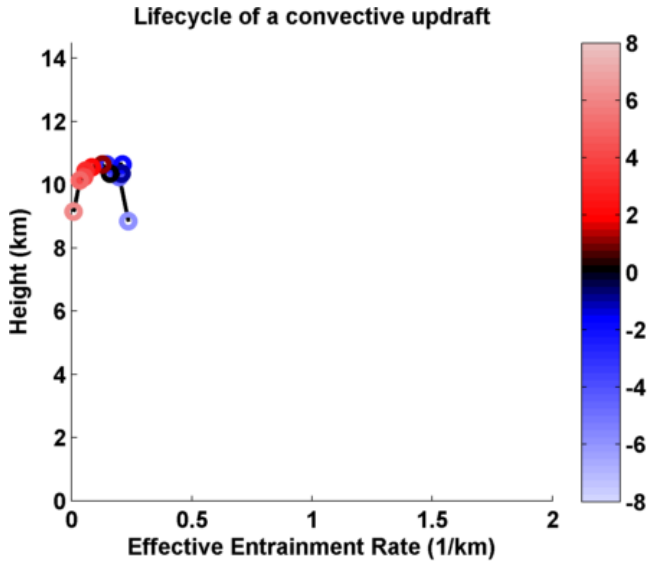

Figure 4.11. As in Figure 4.9, but now for the characteristic λ_w vs CTH for the 3-D subensembles over time for the 4-D cloud illustrated on the RHS of Figure 4.8. Cooler and warmer colors respectively denote the amount of time before and after the subjectively determined "maturity" time in units of 5-minute timeframes. Black represents the "maturity" time for the 4-D cloud.

somewhat steady value of entrainment rate. Figure 4.10 shows evolution over time towards higher and higher effective entrainment rates during the dissipating stage of the 4-D cloud. Figure 4.11 appears simply relatively constant. While these results may be interesting, I cannot draw any general conclusions about the behavior of the 4-D convection from this simple case study. However, if this method were applied over the many hours of simulation time available, an ensemble of many independent 4-D clouds with the same UCTH could be formed. Because of the size of the dataset, this would be computationally taxing, but not impossible. The implications for future research will be discussed in Chapter 5.

CHAPTER 5

DISCUSSION AND CONCLUSIONS

5.1 General characteristics

The general characteristics of convection over the full simulation domain of the Giga-LES at a single time were revealed through a moist static energy (MSE)-based analysis. The field was partitioned into bins of similar MSE and height. The frequency distribution and mass flux over MSE and height space was examined. MSE is conserved for moist adiabatic processes, so it can serve as a proxy for mixing between two parcels of air in the presence of moist convection. Air rising in cumulus updrafts would have constant MSE if it were undiluted by mixing with its environment. The MSE analysis revealed that undilute ascent from the subcloud layer to the upper levels was not observed anywhere in the Giga-LES domain. Furthermore, an idealized convective plume with a constant fractional entrainment rate was shown to approximately match the least diluted points observed in the Giga-LES when it was prescribed an fractional entrainment rate of 10% km^{-1} (Figure 2.2).

Average properties in different MSE bins were plotted to reveal the characteristics of individual points in the simulation. The average vertical velocity distribution (Figure 2.4) reveals some of the dynamics of the simulation. Strong updrafts exist at high values of MSE, representing rising parcels with large buoyancy and low amounts of dilution. Relatively weak downdrafts are frequent at lower values of MSE, near the mean MSE, which is characteristic of the cloud free environment. The average buoyancy distribution (Figure 2.5) supports this view of the vertical velocity

distribution, but shows an interesting pattern of negative buoyancy confined to a region with MSE greater than the domain mean but less than the saturation domain mean MSE. To investigate further, plots of the average cloudy and precipitating condensate distribution were shown. However, these only revealed that the highest values of condensate mixing ratio are found in the least diluted points inside cloudy updrafts.

Plots of total cloud condensate distribution in the simulation revealed more about differences in the thermodynamic state of the air where most of each type of condensate exists in the simulation. By restricting the MSE analysis to particular points in the simulation, differences in the MSE spectrum of mass flux for different dynamical situations became more clear. For example, it was shown that most of the cloudy updraft mass flux exists at values of MSE higher than the saturation MSE $\overline{h}^*$, while most of the cloudy downdraft mass flux exists at values of MSE slightly lower than $\overline{h}^*$. Most of the mass flux in precipitation containing unsaturated downdrafts exists at values of MSE near the domain average, $\overline{h}$. This indicated that the key to understanding the distribution of average buoyancy in MSE space might lie in restricting the MSE analysis to particular regions of the simulation and studying the cloudy downdrafts.

5.2 Characteristics of the near cloud environment

In the study of subsiding shells around deep convection, we used a LES with a large domain (204.8 km $\times$ 204.8 km) and identified active and dissipating 3-D cloudy updrafts. We defined the NCE region as a 500-m thick shell around each active cloudy updraft. We used MSE to classify the air in the active cloudy updrafts and their NCEs across a spectrum from cloudy updraft air to environment air. We refer to the set of parcels with MSE values higher than those in the environment but less than $\overline{\text{MSE}}^*$ as composing the "buoyancy sorting" region in the context of our MSE versus height histograms (Figures 3.3 - 3.6). Most of the NCE is composed of parcels in that region

of MSE space (Figure 3.3). Entraining parcels must pass through the NCE as must parcels that detrain from the active cloudy updraft. This lateral mixing produces a buoyancy sorting process in which each resulting mixture is either entrained or detrained depending on its properties (Taylor and Baker, 1991).

We showed that in this defined buoyancy sorting region, both cloudy updrafts and their NCEs have negative buoyancy, but only the NCEs contain subsaturated parcels. A saturation adjustment model of cloud and environment mixtures reproduces the pattern of negative buoyancy as well as that of decreasing relative humidity with decreasing MSE by requiring evaporative cooling (Figure 3.5). This is consistent with the buoyancy sorting view that parcels detrained into the NCE will be those with negative buoyancy due to evaporation of cloud condensate and vertical velocity less than some threshold (Bretherton et al., 2004). This is also consistent with the properties that HJ08 used to define subsiding shells around shallow cumulus updrafts: a region a few hundred meters thick enveloping the updraft with negative vertical velocity caused by negative buoyancy that is associated with evaporative cooling. Therefore, we conclude that subsiding shells exist in the NCE of the deep convection in the Giga-LES.

The total mass flux in the NCE is negative and is a sizable fraction of the positive total mass flux at a given height in the active clouds, about 50% for NCEs of shallow cumulus at 1.5 km height (Figure 3.8). This compares well with the simulations and observations in (Heus et al., 2009). For cumulus congestus, we calculate a compensating mass flux of about 25% for the NCEs depending on the chosen level. Finally, for deep convective updrafts, the compensating mass flux in the NCEs is about 5% to 10% at a given level. This small value for deep convective NCEs may be due to at least two effects. Heus et al. (2009) note that the mass flux in the subsiding shell is proportional to the area of the shell region, and that this area is proportional to the perimeter of the cloud edge. Therefore, variation of the perimeter to area ratio, a measure of the fractal nature of the cloud edge, may explain variation

in the compensating subsiding shell mass flux between shallow and deep convective NCEs. Furthermore, even though deep convective updrafts contain parcels with higher MSE values and larger positive vertical velocities than those in shallow convective updrafts, each of their NCE regions have similar magnitudes of negative total mass flux. Therefore, similar values of negative vertical velocity in the NCEs of shallow and deep convection can explain the decreasing amount of updraft mass flux compensated for by the subsiding shells in deep convective NCEs.

A subsiding shell is a new cloud structure under study. Recent research has highlighted the importance of the properties of the NCE in determining the process of dilution and entrainment of mass into shallow cumulus clouds (Dawe and Austin, 2011). Additionally, the buoyancy sorting view of detrainment and entrainment has been successfully implemented as a parameterization for shallow cumulus convection (Bretherton et al., 2004). Studying the properties of the subsiding shell in the NCE of cumulus convection may bring more insight to the development of buoyancy sorting parameterizations. Future research may focus on links between the NCE region and the cooling and moistening of the large-scale environment due to detrainment of mass by clouds through the subsiding shell, as well as effects on subsidence warming and drying in the far environment. In this paper, we have demonstrated that a subsiding shell like that observed around shallow cumulus convection also exists in the NCE around active growing and mature deep convective updrafts. This research has only recently been made possible by the computational advances that have allowed a high-resolution simulation over a domain as large as the Giga-LES.

5.3 Characteristics of 3-D and 4-D clouds

In Chapter 4, I used Equation (2.6) to find the change of MSE with height for convective plumes with constant fractional entrainment rates like those described in AS74. I chose the entrainment rate of the plumes to be such that they matched the top height of 3 randomly selected individual 3-D clouds defined as active 3-D cloudy

updrafts in Section 3.1. I showed that, as expected from previous work (Lin and Arakawa, 1997a), the mean MSE of each individual 3-D cloud is quite different from the MSE profile of each plume. Instead, the MSE of the plume was much closer to the maximum MSE observed in the cloud.

This is consistent with the work of Lin and Arakawa (1997b). They showed that a convective plume defined in AS74 with a particular top height represents the subcloud elements that detrain from clouds at that particular height, not a whole cloud with the same particular height. Recent research has shown that much of the entrainment and detrainment for a cumulus cloud occurs through its lateral boundary at all levels of the cloud (Heus et al., 2008; Romps, 2010). This means that the top height of a cloud might be more related to its population of least diluted subcloud elements, rather than its mean properties.

Investigating this possibility, I define Equation (4.5) for the change of vertical kinetic energy with height for a series of rising parcels. I use this equation to find the profile of vertical kinetic energy for a parcel given the average condensate loaded buoyancy in a simulated 3-D cloud from the Giga-LES. The parcel is given a constant fractional entrainment rate that gives a best-fit between the parcel vertical velocity and the cloud mean vertical velocity. One might consider that a more physically-based method would be to instead find a best-fit between the parcel vertical kinetic energy and cloud mean vertical kinetic energy. However, I show in Figure 4.3 that differences resulting from making either choice are quite small. This method captures variability in the population of least diluted subcloud elements for clouds with different and similar top heights. I show in Figure 4.4 that this method has utility for illustrating the variability of dilution and CTH over the full population of hundreds of thousands of 3-D clouds in the simulation in a single figure. However, it was noted that some of the variability displayed in Figure 4.4 could be due to certain clouds not having reached their ultimate cloud top height (UCTH).

In an effort to discover the UCTH for an individual 3-D cloud, I developed a

method that tracks the location of 3-D clouds and determines if they overlap in space and time, forming a 4-dimensional cloud. I applied this method over an hour of simulation time to obtain a small set of 4-D clouds. These 4-D clouds are shown to have sizes over space and time characteristic of the lifecycle of growing and dissipating convection after Ogura and Takahashi (1971). I performed a case study examining a few different 4-D clouds by breaking them down into 3-D subensembles from each timeframe of the 4-D cloud. I used the framework of the bulk entraining plume with an entrainment rate determined from an iterative method comparing the vertical velocity profile w_p from a series of rising parcels with the 3-D cloud subensemble mean vertical velocity profile $\overline{w_c}$. This resulted in time varying values of bulk characteristic entrainment rate λ_w with instantaneous CTH for individual 4-D clouds, as in Figure 4.11.

It appears that this method holds promise for isolating clouds with similar UCTHs. If a larger set of 4-D clouds were obtained, I could compare the variability of fractional entrainment rate within a group of 4-D clouds with similar UCTHs with the variability between groups of 4-D clouds with different UCTHs. This would answer the question asked in the beginning of Chapter 4, is there any pattern to the dilution characteristics of different types of clouds? The method could be used to answer this question considering other properties as well. If initial cloud base area was investigated instead, for example, this method could be used to determine the relationship between initial cloud base area, fractional entrainment rate, and ultimate cloud top height. Such relationships have long been known to exist in controlled laboratory studies of buoyant plumes (Morton et al., 1956; Turner, 1969). The existence, strength, and variability of such a relationship in simulated clouds is the subject of considerable amounts of recent research concerning the parameterization of cumulus convection for climate models (Neggers et al., 2002; Chikira and Sugiyama, 2010; Romps and Kuang, 2010b). It is possible that this could be a fruitful direction for further research.

5.4 Summary

In summary, the first goal of this work was to understand how the cloudy updraft mass flux in the Giga-LES is distributed through the general framework of fundamental ideas about cumulus parameterization that have been established in the field. This is done through a MSE spectrum and entraining plume-based analysis in Chapters 2, 3, and 4. In particular, in Chapter 2, I characterized the thermodynamic structure, dynamics, and hydrometeor population of the full simulation domain through the MSE and height spectral analysis technique. This led to questions about the relationship between buoyancy and downdrafts in the near cloud environment.

The second goal for this work was to present new insight through a fresh interpretation of established analysis methods. To this end, in Chapter 3, I applied the MSE spectral analysis technique to the near cloud environment of active cloudy updrafts. Through the framework of mixing diagrams and buoyancy sorting processes, I interpreted the results of the MSE analysis as novel evidence for a subsiding shell driven by evaporative cooling in the near cloud environment of deep convection. This resulted in new information about the mass flux in subsiding shells around deep convection.

In further pursuit of these two goals, in Chapter 4, I focused on individual clouds. I presented a new method for characterizing the dilution of a cloud with a constant fractional entrainment rate that was sensitive to the cloud's population of least diluted subcloud elements. This allowed for variability in both CTH and composition of least diluted subcloud elements to be simultaneously examined over thousands of active cloudy updrafts in the simulation. I ended with some results from a new method that tracks 3-D clouds through time to isolate 4-D cloud clusters. This new method has the potential to answer important questions in the study of cumulus convection, as discussed above. Both goals of this work have been accomplished.

REFERENCES

Arakawa, A., 2004: The cumulus parameterization problem: Past, present, and future. *J. Clim.*, **17 (13)**, 2493–2525.

Arakawa, A. and W. H. Schubert, 1974: Interaction of a cumulus cloud ensemble with the large-scale environment: Part I. *J. Atmos. Sci.*, **31 (3)**, 674–701.

Arakawa, A. and C.-M. Wu, 2013: A unified representation of deep moist convection in numerical modeling of the atmosphere: Part I. *J. Atmos. Sci.*, **70**, 1977–1992, doi:http://dx.doi.org/10.1175/JAS-D-12-0330.1.

Aristotle, 1984: *The complete works of Aristotle*, J. Barnes, Ed., Princeton University Press, Vol. 1, 1256 pp.

Bjerknes, J., 1938: Saturated-adiabatic ascent of air through dry-adiabatically descending environment. *Quart. J. Roy. Meteor. Soc.*, **64 (275)**, 325–330.

Bretherton, C. S., P. N. Blossey, and M. Khairoutdinov, 2005: An energy-balance analysis of deep convective self-aggregation above uniform SST. *J. Atmos. Sci.*, **62**, 4273–4292.

Bretherton, C. S., J. R. McCaa, and H. Grenier, 2004: A new parameterization for shallow cumulus convection and its application to marine subtropical cloud-topped boundary layers. Part I: Description and 1D results. *Mon. Wea. Rev.*, **132**, 864882.

Bretherton, C. S. and P. K. Smolarkiewicz, 1989: Gravity waves, compensating subsidence and detrainment around cumulus clouds. *J. Atmos. Sci.*, **46 (6)**, 740–759.

Chikira, M. and M. Sugiyama, 2010: A cumulus parameterization with state-dependent entrainment rate. Part I: Description and sensitivity to temperature and humidity profiles. *J. Atmos. Sci.*, **67 (7)**, 2171–2193.

Dawe, J. T. and P. H. Austin, 2011: The influence of the cloud shell on tracer budget measurements of LES cloud entrainment. *J. Atmos. Sci.*, **68**, 2909–2920, doi:10.1175/2011JAS3658.1.

de Roode, S. R. and C. S. Bretherton, 2003: Mass-flux budgets of shallow cumulus clouds. *J. Atmos. Sci.*, **60 (1)**, 137–151.

de Rooy, W. C., et al., 2013: Entrainment and detrainment in cumulus convection: An overview. *Quart. J. Roy. Meteor. Soc.*, **139**, 1–19, doi:10.1002/QJ.1959.

Donner, L. J., 1993: A cumulus parameterization including mass fluxes, vertical momentum dynamics, and mesoscale effects. *J. Atmos. Sci.*, **50**, 889–906.

Dorrestijn, J., D. T. Crommelin, P. A. Siebesma, and H. J. J. Jonker, 2013: Stochastic parameterization of shallow cumulus convection estimated from high-resolution model data. *Theor. Comput. Fluid Dyn.*, **27**, 133–148.

Emanuel, K. A., 1994: *Atmospheric convection*. Oxford University Press.

Fierro, A. O., J. Simpson, M. A. LeMone, J. M. Straka, and B. F. Smull, 2009: On how hot towers fuel the Hadley cell: An observational and modeling study of line-organized convection in the equatorial trough from TOGA COARE. *J. Atmos. Sci.*, **66 (9)**, 2730–2746.

Freeland, C. A., 1999: Scientific explanation and empirical data in Aristotle's Meteorology. *Aristotle: Logic and metaphysics*, L. P. Gerson, Ed., Taylor & Francis US, Vol. 2, 177–208.

Garrett, T. J., 2012: Modes of growth in dynamic systems. *Proc. Roy. Soc. A*, **468 (2145)**, 2532–2549.

Gedzelman, S. D., 1989: Cloud classification before Luke Howard. *Bull. Am. Meteor. Soc.*, **70**, 381–467.

Gerard, L., 2007: An integrated package for subgrid convection, clouds and precipitation compatible with meso-gamma scales. *Quart. J. Roy. Meteor. Soc.*, **133**, 711–730.

Heus, T. and H. J. J. Jonker, 2008: Subsiding shells around shallow cumulus clouds. *J. Atmos. Sci.*, **65**, 1003–1018.

Heus, T., J. Pols, C. Freek, J. Jonker, J. Harm, A. Van den Akker, E. Harry, and D. H Lenschow, 2009: Observational validation of the compensating mass flux through the shell around cumulus clouds. *Quart. J. Roy. Meteor. Soc.*, **135 (638)**, 101–112.

Heus, T., G. van Dijk, H. J. J. Jonker, and H. E. A. Van den Akker, 2008: Mixing in shallow cumulus clouds studied by lagrangian particle tracking. *J. Atmos. Sci.*, **65**, 2581–2597.

Holton, J. R., 1992: *An introduction to Dynamic Meteorology*. Academic press, 504 pp.

Howard, L., 1803: On the modification of clouds, and on the principles of their production, suspension and destruction. *Philosophical Magazine*, **17 (65)**, 5–11, doi:10.1080/14786440308676365.

Jonas, P. R., 1990: Observations of cumulus cloud entrainment. *Atmos. Res.*, **25**, 105–127.

Jonker, H. J. J., T. Heus, and P. P. Sullivan, 2008: A refined view of vertical mass transport by cumulus convection. *Geophys. Res. Lett.*, **35**, L07810, doi: 10.1029/2007/GL032606.

Khairoutdinov, M. and D. Randall, 2003: Cloud resolving modeling of the ARM summer 1997 IOP: Model formulations, results, uncertainties, and sensitivities. *J. Atmos. Sci.*, **60**, 607–625.

Khairoutdinov, M. F., S. K. Krueger, C.-H. Moeng, P. Bogenschutz, and D. A. Randall, 2010: Large-eddy simulation of maritime deep tropical convection. *J. Adv. Model. Earth Syst.*, **1**, doi:10.3894/JAMES.2009.1.15.

Khairoutdinov, M. F. and D. A. Randall, 2006: High-resolution simulation of shallow-to-deep convection transition over land. *J. Atmos. Sci.*, **63**, 3421–3436, doi:10.1175/JAS3810.1.

Kuang, Z. and C. S. Bretherton, 2006: A mass-flux scheme view of a high-resolution simulation of a transition from shallow to deep cumulus convection. *J. Atmos. Sci.*, **63**, 1895–1909, doi:10.1175/JAS3723.1.

Lin, C. and A. Arakawa, 1997a: The macroscopic entrainment processes of simulated cumulus ensemble. Part I: Entrainment sources. *J. Atmos. Sci.*, **54**, 1027–1043.

Lin, C. and A. Arakawa, 1997b: The macroscopic entrainment processes of simulated cumulus ensemble. Part II: Testing the entraining-plume model. *J. Atmos. Sci.*, **54**, 1044–1053.

Morton, B. R., G. Taylor, and J. S. Turner, 1956: Turbulent gravitational convection from maintained and instantaneous sources. *Proceedings of the Royal Society of London*, **234 (1196)**, 1–23.

Neggers, R. A. J., A. P. Siebesma, and H. J. J. Jonker, 2002: A multiparcel model for shallow cumulus convection. *J. Atmos. Sci.*, **59 (10)**, 1655–1668.

Ogura, Y. and T. Takahashi, 1971: Numerical simulation of the life cycle of a thunderstorm cell. *J. Clim.*, **99 (12)**, 895–911.

Riehl, H. and J. S. Malkus, 1958: On the heat balance in the equatorial trough zone. *Geophysica*, **6**, 503–538.

Rodts, S. M. A., P. G. Duynkerke, and H. J. J. Jonker, 2003: Size distributions and dynamical properties of shallow cumulus clouds from aircraft observations and satellite data. *J. Atmos. Sci.*, **60**, 1895–1912.

Romps, D. M., 2010: A direct measure of entrainment. *J. Atmos. Sci.*, **67**, 1908–1927.

Romps, D. M. and Z. Kuang, 2010a: Do undiluted convective plumes exist in the upper tropical troposphere? *J. Atmos. Sci.*, **67 (2)**, 468–484.

Romps, D. M. and Z. Kuang, 2010b: Nature versus nurture in shallow convection. *J. Atmos. Sci.*, **67 (5)**, 1655–1666.

Romps, D. M. and Z. Kuang, 2011: A transilient matrix for moist convection. *J. Atmos. Sci.*, **68**, 2009–2025, doi:10.1175/2011JAS3712.1.

Siebesma, A. and J. Cuijpers, 1995: Evaluation of parametric assumptions for shallow cumulus convection. *J. Atmos. Sci.*, **52 (6)**, 650–666.

Siebesma, A. P., 1998: Shallow cumulus convection. *Buoyant Convection in Geophysical Flows*, E. J. Plate, E. E. Fedorovich, X. V. Viegas, and J. C. Wyngaard, Eds., Kluwer Academic Publishers, 441–486.

Song, X., G. J. Zhang, and J.-L. Li, 2012: Evaluation of microphysics parameterization for convective clouds in the NCAR Community Atmosphere Model CAM5. *J. Clim.*, **25**, 8568–8590.

Taylor, G. R. and M. B. Baker, 1991: Entrainment and detrainment in cumulus clouds. *J. Atmos. Sci.*, **48**, 112–121.

Turner, J. S., 1969: Buoyant plumes and thermals. *Annual Review of Fluid Mechanics*, **1**, 29–44.

Wallace, J. M. and P. V. Hobbs, 2006: *Atmospheric science: an introductory survey.* Academic press, 504 pp.

Warner, J., 1970: On steady-state one-dimensional models of cumulus convection. *J. Atmos. Sci.*, **27**, 1035–1040.

Yanai, M. and R. H. Johnson, 1993: Impacts of cumulus convection on thermodynamic fields. *The Representation of Cumulus Convection in Numerical Models, Meteor. Monogr.*, Amer. Meteor. Soc., 39–62.

Zhang, G. J. and N. A. McFarlane, 1995: Sensitivity of climate simulations to the parameterization of cumulus convection in the Canadian Climate Centre general circulation model. *Atmos.- Ocean.*, **33 (3)**, 407–446.

Zipser, E. J., 2003: Some views on hot towers after 50 years of tropical field programs and two years of TRMM data. *Meteorological Monographs*, **29 (51)**, 49–58.